JMEST
Journal of Marine Earth Science and Technology
Volume 1 Issue 1
Sept - Dec 2020
ISSN 2774-5449

Computational Analysis On Heave And Pitch Motions Performance Of A Hydrofoil Ship

The Application Of Combination Of Solid Boxes
And Air Bags To Support The Unsinkable Small Passenger Boat

Application Of Upward Continuation Filter For Geomagnetic Data Interpretation In Gondang, Bojonegoro Area

GNSS Meteorology And Land Subsidence Of Heavy Rainfall In Jakarta On January 2020 ,1

Characteristic Of Spent Bleaching Earth Substitution In Limestone As Landfill Material

itspress

JMEST
Journal of Marine-Earth Science and Technology

Journal of Marine-Earth Science and Technology
Volume 1 Issue 1.September - December 2020. ISSN. 2774 5499

Editor's Note :

In the fast-growing of science and technology in marine-earth related topics, we would like to launch a new international journal entitled Marine-Earth Science and Technology Journal (JMEST). The new journal is aimed as a media communication amongst scientists and engineers in the fields of marine and earth science and technology and will receive research and technical papers to be reviewed by our editors and reviewers. The JMEST will be issued three times a year and the first issue consists of 5 (five) papers from Malaysia and Indonesia.

Scopes of Journal :

Marine Science, Naval Architecture, Ship Production Technology, Marine Engineering, Marine Technology, Marine Transportation and Logistics, Ocean Renewable Energy, Earth Science, Physical Oceanography, Ocean and Atmospheric Interaction, Geology and Marine Geology, Geothermal Engineering, Geophysics, Disaster Management and Mitigation, Coastal Environmental Protection.

Table Of Contents

APPLICATION OF UPWARD CONTINUATION FILTER FOR GEOMAGNETIC DATA INTERPRETATION IN GONDANG, BOJONEGORO AREA

Yolanda Mustika BOHAL, MARIYANTO, and Widya UTAMA
Department of Geophysical Engineering, Institut Teknologi Sepuluh Nopember
e-mail: widya@geofisika.its.ac.id

ABSTRACT

In the Gondang area, Bojonegoro, East Java, there were manifestations of hot springs and mud pools. This can be an indication of certain geological conditions. The description of these conditions can be done by measuring the geomagnetic method. A total geomagnetic anomaly has been generated through some geomagnetic values recorded in the region, which has been corrected using IGRF correction and diurnal correction. These steps were done to reduce external influences on the real value of the data. This research will use several variations of values in the Upward Continuation filter and one of them will be chosen to proceed as a model. Upward Continuation Filter is a process of transforming potential field data from a flat plane towards the higher plane. The purpose of this study is to compare the results of contour maps on several variations of the Upward Continuation value, to obtain the results of the separation of residual and regional anomalies using the Upward Continuation method, and to determine the value of the susceptibility distribution of inversion modeling in the Gondang region, Bojonegoro. Based on the results of data processing, it is known that the upward continuation value used is 100mdatum with a magnetic intensity value in the regional anomaly of 106.5 nT to 509.0. While the value of the residual anomaly is -232.1 nT to 159.4 nT. The 3D model was made using this residual anomaly which shows the low susceptibility distribution value in the range of -0.0298 to -0.0135 SI around the manifestation area, whereas the high susceptibility value has a value range of 0.0114 to 0.0466 SI interpreted as rock intrusion. Rock intrusion occurs within the area around the manifestation of mud pools.

Keywords : *Geomagnetic Anomaly, Susceptibility, Upward Continuation*

1. Introduction

The geomagnetic method is one of the geophysical methods used to model subsurface conditions. Data measurement is expected to be able to show the actual geological conditions. In the case study of Gondang, Bojonegoro, East Java, the exemplified of hot springs and mud pools were manifested. This can be an indication of certain geological conditions (Khalil, 2016). This depiction can be seen through variations in the distribution of rock susceptibility namely, the ability to accept the magnetic properties of the earth's magnetic field. This research is expected to produce susceptibility distribution from 3D inversion modeling in Gondang, Bojonegoro. Previously, the geomagnetic method was successfully used to identify the susceptibility distribution (Maubana, W., et al, 2019)

The measurement will produce a total magnetic anomaly that can be separated into regional magnetic anomalies and residual magnetic anomalies. The usual separation method used is Upward Continuation. The separation with Upward Continuation has several reflection variations which are themain source in the interpretation of geomagnetic data, hence this is the reason why this study becomes interest-

ing. Thus, this study also discusses the comparison of the results of several Continuation variations.

Geomagnetic data interpretation has been carried out to inversion modeling of the results of the separation of local regional anomalies with Upward Continuation conducted by Maubana et al (2019). The research succeeded in identifying the geothermal reservoir through geomagnetic data. Based on the succeed of several previous studies, the authors are interested in applying the Upward Continuation filter to interpret geomagnetic data in Gondang, Bojonegoro

2. Geological Setting

This research area is located in Gondang, Bojonegoro, East Java. The physiography of the study area is the Kendeng Zone in the south, which consists of rough hills with steep slopes. According to Van Bemelen (1949), this zone is a limestone mountain range in the northern part of Java Island which stretches from east to west. This research area is located above several formations. Based on the references from Rahardjo Wartono (2007), the stratigraphy formation of this research area starts from the oldest one, which called the Kerek Formation. This unique formation has its lithology in the form of repetition of interlocking claystone, marl, sandstone tuff sandstone, and sandstone tuff. This iteration shows a typical sedimentary structure known as graded bedding.

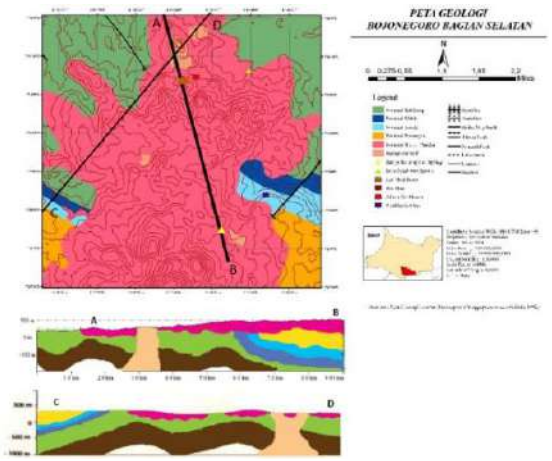

Fig 1. Geological Map of Gondang (Bemellen, V., 1949)

Above the Kerek Formation, there is the Kalibeng Formation which consists of two divided parts, the top and the bottom. At the bottom, there are several thin layers of sandstone that are heading towards the western part of Kendeng which develops into a stream of sediment flow and identified as a member of the lot. The upper formation of the Kalibeng is referred to the Pliocene-age Sonde Formation which composed of Klitik Members located above the Sonde Formation. This formation consists of a yellowish-white calciteite lithology unit. The top formation is the Pucangan Formation which develops as volcanic facies and black clay facies. Its volcanic facies develop as lava deposits that hitch a ride above the Kalibeng Formation. In the study area, volcanic breccias located at the manifestation location were found in the Banyukuning and Jari hot spring pools. In the study area, there

is rock intrusion which estimated to be a pyroxene andesite that cuts along the Kalibeng formation towards the volcanic breccia facies.

3. Methodology

3.1. Measurement of Magnetic Data

The data in this study were obtained through a process of data acquisition and retrieval carried out on September 2, 2019 to September 9, 2019 at 94 measurement points scattered in several villages in Gondang District, Bojonegoro with a GSM-19T Proton Magnetometer. The acquisition design used in this study is as follows:

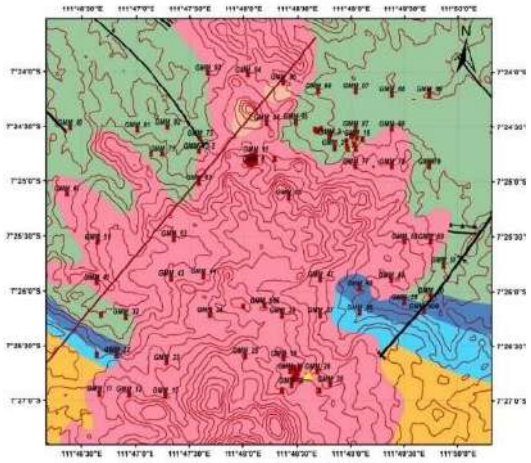

Fig.2. The measurement data point of the research in the study area

3.2. Magnetic Data Processing

The magnetic data that has been collected will be processed by correcting it first due to the many factors that affect the value of magnetic intensity. Corrections to be made are daily corrections and IGRF corrections (Utama, W., et al, 2016)

IGRF correction can be done automatically via the NOAA website or software such as Oasis Montaj. Meanwhile, the daily correction needs to be calculated by interpolating the intensity values that are

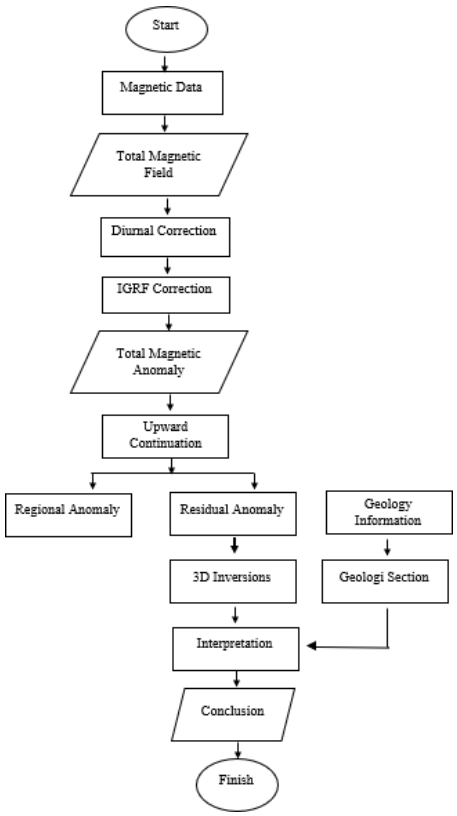

Fig. 3. Flowchart of Research

base according to the time available on the rover or mobile device used. (Lutfi, 2017)

$$H_a = \frac{(H_{max} - H_{min})}{2} \quad (1)$$

where H_a is the reference of magnetic field value to get the diurnal correction value. H_{max} is the maximum magnetic field value recorded by Proton Procession Magnetometer (PPM) while H_{min} is the minimum magnetic field value.

$$H_{kh} = H_a - H_h \quad (2)$$

H_{kh} is the daily correction of the magnetic field and Hh is the value of the daily magnetic field. After getting the daily value of the magnetic field correction, an interpolation is performed at each time the data is retrieved on the rover.

$$H_{th} = H_l + H_{kh} \quad (3)$$

where H_{th} is a magnetic field that has been corrected daily at the time of measurement by the rover.

The corrected result is a total anomaly which will be filtered with upward continuation. In this filter, the amount to be used will be entered manually according to the desired height, but this can be seen with the noises that have been lost. In the geomagnetic method of data processing, this process is used as a low filter to eliminate unrelated topography to the survey so that the anomaly results obtained are more clearly visible (Rekswanda, 2017).

$$U(x, y, z_0 - \Delta z) = \frac{|\Delta z|}{2\pi} \cdot \int_{-\alpha}^{\alpha} \int_{-\alpha}^{\alpha} \frac{(x', y', z_0)}{R^3} dx' dy'$$

with $\mathbf{R} = |x - y'|^2 + |y - y'|^2 + \Delta z^2$ and $\mathbf{U}(x, y, z_0)$ = value of the potential field in the continuation yield field, while Δz is distance or height removal and $U(x', y', z_0)$ is the value of the potential field in the actual field of observation $(\Delta z = 0)$.

If the potential field, for example, the U field is measured on the surface $z = z_0$ and has a Fourier transform $F[U]$. The Fourier transform representation for equation (4) can be found by transforming both sides of the equation into the Fourier domain and applying the Fourier convolution (Blakely, 1995).

$$F[U_u] = F[U]F[\psi_u] \tag{5}$$

where $F[U_u]$ is a fourier transform of a field that is continued upwards. All that is needed is an analytical expression for $[\Psi_u]$ which can be found from the forier transfer in equation (4). Need to know that

$$\psi_u(x, y, \Delta z) = -\frac{1}{2\pi} \frac{\partial}{\partial \Delta z} \frac{1}{r} \tag{6}$$

where $r = \sqrt{x^2 + y^2 + \Delta z^2}$. . Therefore, fourier transform from the equation (6) is

$$\begin{aligned} F[\psi_u] &= -\frac{1}{2\pi} \frac{\partial}{\partial \Delta z} F\left[\frac{1}{r}\right] \\ &= -\frac{\partial}{\partial \Delta z} \frac{e^{-|k|\Delta z}}{|k|} \\ &= e^{-\Delta z|k|} \quad , \Delta z > 0 \end{aligned} \tag{7}$$

Then it is necessary to do a comparison between the results of each data.

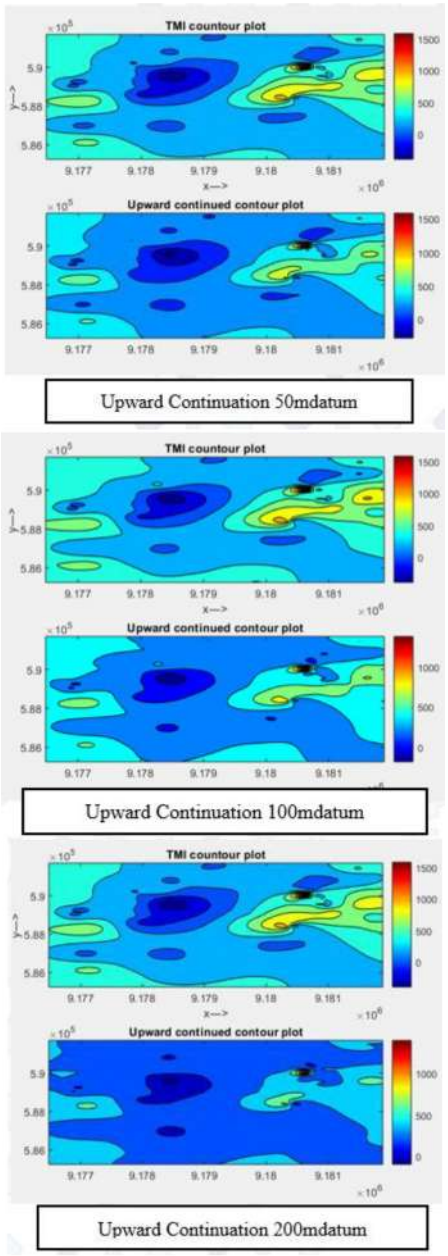

Fig 4. Comparison of datums in the Upward Continuation filter

In this study, regional anomalies were obtained through a map of total magnetic anomalies that had been continued upwards. The next step is to get a map of residual anomalies by reducing total manic anomalies with regional anomalies. This reduction is done with the Grid Math feature on the *Oasis Montaj software.*

It also made a geological cross-section with an incision that passes through 2 points of manifestation and also 3D modeling inversion. 3D modeling inversion was using the VOXI feature on Oasis Montaj. The calculation of matrix inversion on this inversion uses the Singular Value Decomposition or SVD technique (Press et al, 1987) which is relatively more stable. In this technique, certain values can be ignored or considered zero and not included in the calculation of solutions (Grandis H. 2009). This calculation involves the norm model and also the norm data where both norms (Λ) are searched for the optimum value.

In this process, the model fits in observational data and also to fit the existing geological conditions. It is necessary to do several iterations to produce optimum results when the model approaches the observation value as well as its geology.

4. Result and Discussion

The total magnetic anomaly produced in Figure 5 shows the value of the variation of magnetic intensity from the range of 44595 nT to 44610. Low-intensity values (tend to be blue) are found in the manifestation areas such as mud pools, Selogajah, and also Banyukuning. Manifestations of hot water and mud can be categorized as diamagnetic, where susceptibility is very low due to the number of electrons being even and paired so that the magnetization level is low, which is required with low-intensity values in the measurement results of this study.

The comparisons between 50, 100, and 200 m datum are obtained through trial and error results until anomalous maps show fairly clear points in areas of interest, especially at 3 points of manifestation.

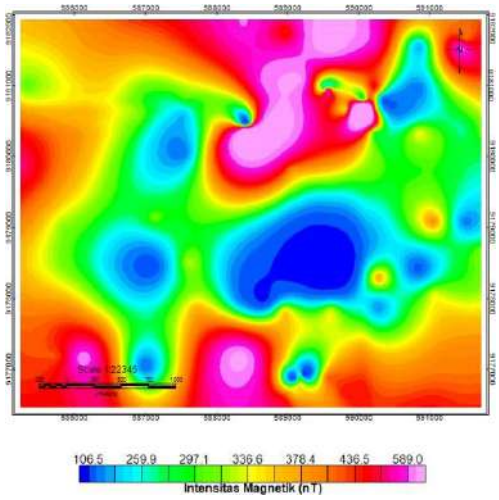

Fig 5. Total Magnetic Anomaly Map in Gondang

Between the three datum values, the writer visually determines that the 100mdatum value is appropriate to proceed in modeling. The choice of 100 m datum (figure 4) for the upward continuation value because it has removed residual effects on the total intensity value compared to the 50m datum lift value, but it is also does not eliminate much of the information intensity value of the data as in the appointment with a 200mdatum value. These upward continuation maps illustrate changes in anomalous characters with increased observations of the distance of the magnetic source, and are also useful as a low pass filter. Thus, continued data up to 100m provides an excellent integrated view of the study area that is not distorted by local anomalies, high amplitude, and high gradients from magnetic sources in the shallows of the study area. It is clear that the weakening of shallow source anomalies in the upward continuation process enables a clearer or enhanced view of deeper anomalous sources (Blakely, 1996).

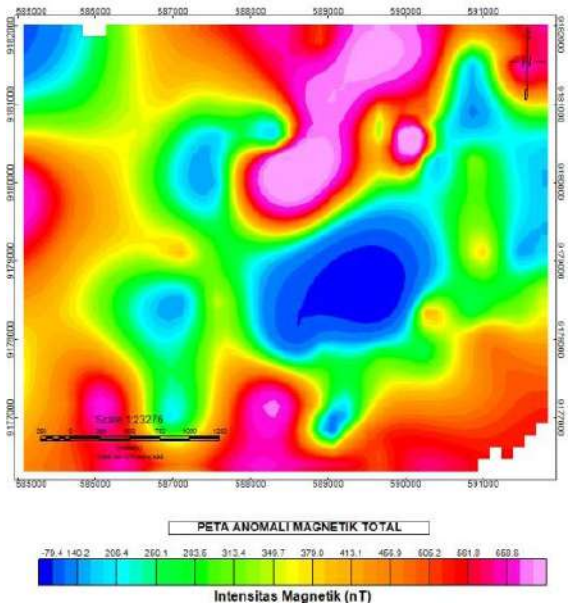

Fig 6. Regional Magnetic Anomaly Map in Gondang

Residual anomalies explain the distribution of subsurface geological structures clearer and more specifically, hence that is why this study uses a residual magnetic anomaly since it is considered as the most suitable for the interpretation of magnetic anomalies. The residual anomaly values depicted in Figure 7 show areas of low intensity with a range of -232 nT to -110 nT. This can be interpreted with low susceptibility by the low magnetism of the mud and hot water types.

A low susceptibility value can occur in the event of demagnetization. Manifestations in hot tubs have quite high temperatures.

Susceptibility has an influence on, namely the smaller and negative value of susceptibility in rocks, then, in theory, these rocks are diamagnetic at fairly high temperatures. This is because when rocks are diamagnetic, the electron shells will be completed and filled with paired electrons.

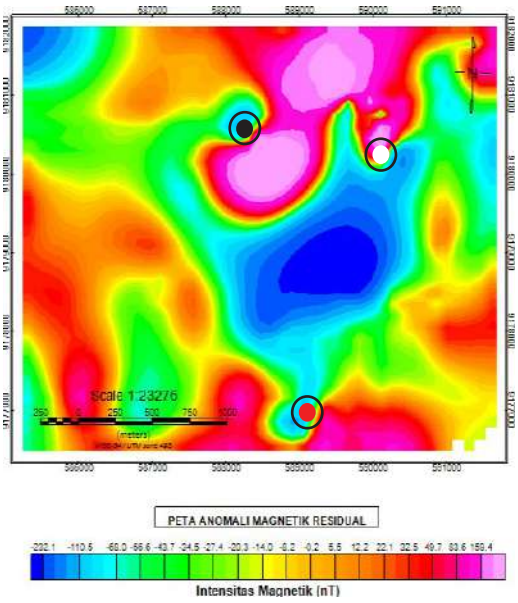

Legenda :

Mud Volcano Selogajah Banyukuning

Fig 7. Residual Magnetic Anomaly Map in Gondang

If it is influenced by an external magnetic field, the spin of electrons will produce the direction of the magnetic moment that is opposite to the direction of the external field strength and produce a resultant which directed towards negative direction, so that a susceptibility relationship to a constant value can be obtained. Therefore, the low susceptibility value can be assumed as a manifestation of mud and hot water.

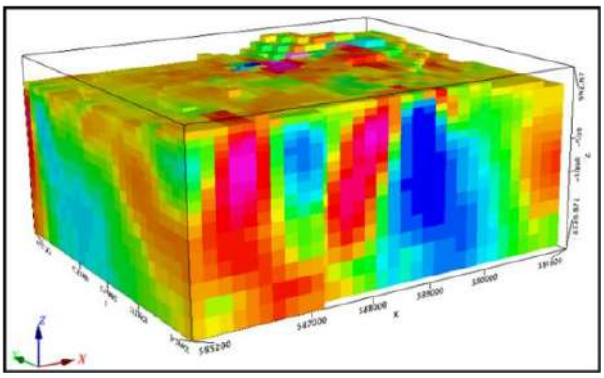

Fig 8. Results of 3D inversion of residual anomalies in the study area

The residual anomaly map is the modeled inversely (figure 8). From the results of magnetic data processing, 3D modeling interpretation

can be made especially on the path connecting the manifestations of Jari and Banyukuning hot spring pools which can be seen through slicing (figure 9). These manifestations indicate certain conditions below the surface. This can be seen through the results of modeling that has been done and through the validation of the geological incision as well. Based on the track above (figure 9) it can be assumed that the rock intrusion is characterized by a susceptibility value of 0.0084-0.0446 SI (pink to dark red). This intrusion stone usually regarded as pyroxene andesite because the rock susceptibility is very high. In addition, compared to geological incisions, there is rock intrusion around the location of intrusion manifestations of mud pools and Selogajah. This can be interpreted as the existence of mud pools and hot tubs due to the correlation between events and rock intrusion.

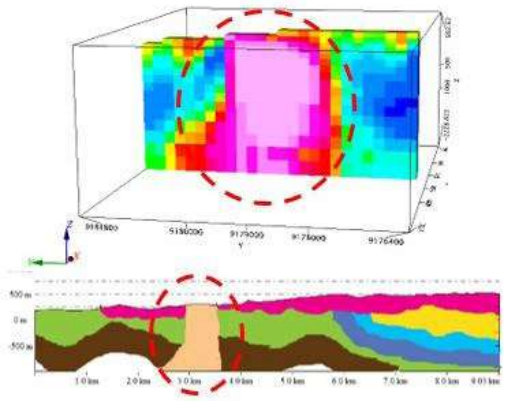

Fig 9. Comparison of geological section with the inversion model of the Jari mud volcano - Banyukuning

In addition to the path above, there is also an incision that crosses a mud pool and Selogajah (figure 10) showing rock intrusions that are marked by red to pink. In accordance to what has been mentioned above, this value has a high susceptibility with a range of 0.0114 to 0.0466 SI. If reflected in the geological conditions, the intrusive rocks are pyroxene andesite, whereas the rocks around it are shown at -0.0023 to 0.0068 SI which can be predicted to enter the Kerek formation with tuff sandstone.

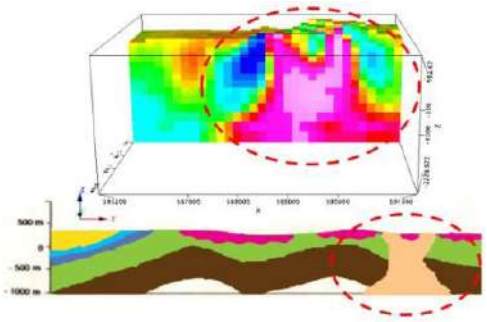

Fig 10. Comparison of geological incisions with the inversion model of the Selogajah Hot-Jari Mud Volcano

In the model above (figure 10) the upper layer susceptibility value is assumed to be breccia volcanic rock, which can be found in the top layer at the study site (Kendeng Zone) marked in blue. In this inversion model, the blue value has a susceptibility value of -0.0319 to -0.0057. This very small magnetic value can occur due to demagnetization. The green color in the inversion model can be interpreted as a Kalibeng formation with susceptibility value of -0.0061 to 0.0012. As previously explained, the intrusion of rocks with this path is quite clearly visible with the pink symbol on the inversion model and the beige color on the geological incision. Likewise, the Kerek formation as the oldest formation in the study area can be clearly seen more in the geological incision by comparing the inversion model at the susceptibility value of -0.0033 SI.

5. Conclusions

The 100m datum value applied in part to the upward continuation value of the total magnetic anomaly is the most suitable result as a regional anomaly because it removes residual effects without losing geological information. The results value of the upward continuation is 106.5 nT to 509.0 nT. Meanwhile, results with 50mdatum still show noises and results with 200m datum eliminates too much geological

information. After obtaining a regional anomaly, a residual anomaly can be obtained by reducing the total magnetic anomaly against the regional anomaly. The residual anomaly magnetic intensity value is -232.1 nT to 159.4 nT

Low rock susceptibility distribution values based on inversion models are in areas of manifestation with values ranging from 0.0298 to -0.0135 SI and high susceptibility values with values ranging from 0.0114 to 0.0466 SI which can be interpreted as andesite pyroxene intrusion rocks. Mapping subsurface conditions shows the intrusion of rocks which interpreted as andesite pyroxene as the youngest formation, the formation underneath is volcanic breccia and Kerek formation which is the oldest formation in the study area.

References

[1]. Bemmelen Van, R.W. (1949), The Geology of Indonesia. Martinus Nyhoff, Netherland: The Haque.

[2]. Blakely, R.J., (1996) Potential Theory in Gravity and Magnetic Application, Cambridge University Press.

[3]. Husein, S. (2013), Perkembangan Tektonik Pegunungan Selatan Yogyakarta: dari busur volkanik hingga patahan bongkah, sebuah kontribusi pemikiran. Presentasi pada Seminar Nasional memperingati 30 tahun Stasiun Lapangan Geologi 'Prof. R. Soeroso Notohadiprawiro' Bayat, Jurusan Teknik Geologi FT UGM.

[4]. Khalil, M.H. (2016), "Subsurface Faults Detection Based on Magnetic Anomalies Investigation: A Field Example at Taba Protectorate, South Sinai", Journal of Applied Geophysics, Vol.131, hal. 123– 132.

[5]. Luthfi,I., (2017) Aplikasi Metode Magnetik Sebagai Lagkah Awal Eksplorasi Panasbumi. Penerbit ITB, hal 25-27.

[6]. Maubana, W., Maryanto, S., Utami, I.W., Nadir, A. (2019), Reservoir Magnetic Anomaly at Geothermal Area of Mount Pandan, East Java, Indonesia. International Journal of Renewable Energy Research. Vol. 9, No. 2.

[7]. Press, W.H., Falennery,B.P., Teukolsky, S.A., Vetterling, W.T., 1987, Numerical recipes : The art og scientific computing, Cambrigde University Press.

[8]. Rahardjo, Wartono. (2004), "Buku Panduan Ekskursi Geologi Regional Pegunungan Selatan dan Zona Kendeng". Jurusan Teknik Geologi

[9]. Reynolds, J.M. (2011). "An Introduction to Applied and Environtmental Geophysics". West Sussex. John Wiley& Sons, Ltd.

[10]. Telford, W.M., L.P Geldart., R.E Sheriff. (2004), "Applied Geophysics Second Edition". Edinburgh: Cambridge University Press

[11]. Utama, W., Warnana,D. D., Hilyah, A., Bahri, S., Syarifuddin, F. dan Rismayanti, H. F. (2016), "Eksplorasi Untuk Penentuan Keberadaan Pipa Air Bawah Permukaan Bumi". Jurnal Geosaintek, hal 157-16

THE APPLICATION OF COMBINATION OF SOLID BOXES AND AIR BAGS TO SUPPORT THE UNSINKABLE SMALL PASSENGER BOAT

Wolter R Hetharia, Eliza R de Fretes, Fella Gaspersz, Jandri Louhenapessy
Department of Naval Architecture, Faculty of Engineering, Pattimura University, Ambon
e-mail : hethariawr@yahoo.com

ABSTRACT

Small fast passenger boats serve to carry passengers at certain routes particularly in short distance between the islands. The passengers preferred those transport modes due to its short travel time. In fact, there are many accidents occur during boat operation which end up with the loss of life and materials at sea. An intensive study was executed by the authors with the purpose to obtain an unsinkable boat. The boat data of existing boats were collected and be used for re-designing process. During the design process, some solid boxes, expanded bags were provided inside boat to reduce the incoming water. Meanwhile, the bags were fitted outside the boat (side floater) to provide additional buoyancy and righting moment for stability performance. A boat model was developed and tested to confirm the design results. In addition, a full-scale boat was developed and equipped with solid boxes, air bags and side floaters. The theoretical computation and extrapolated results from model proved that the required volume for inside solid boxes and air bags are 1.213 m^3 and 0.511 m^3 respectively. Meanwhile, the required volume of outside air bags is 0.357 m^3. It was found that the total boat weight, passengers and incoming water of 4.259 tons are balanced by weight displacement of 5.025 tons. There was reserve buoyancy of 0.766 tons that supports the boat to be float and side floaters to prevent the boat from capsize. The result of sea trial showed that with all loading conditions the boat was still afloat (unsinkable).

Keywords : *solid boxes, air bags, unsinkable*

INTRODUCTION

The contribution of small fast boats to serve inter-island transport is favorable for the passengers due to the short travel time. In many archipelago regions this kind of transportation mode is preferred due to the small input passengers on board and easy operation instead of bigger ships. In fact, those boats operate in the open sea with bad conditions such as high wind and big waves. Many accidents occur for those small boats such as sinking and capsizing which end-up with the loss of life and materials at sea (Basarnas, 2016; Hetharia, 2014; Hetharia, 2018).

Continuous studies concerning this issue have been conducted by several authors. The first study was related to tuna long-line fishing boat (Hetharia, 2008; Hetharia, 2017; Hetharia 2018). In this study the boat was provided by inserting light solid boxes on board. The purpose of applying solid boxes is to reduce the incoming water on board. The sea trial has proved that the boat was still afloat even it was filled fully by sea water. In addition, the boat still afloat (unsinkable) in capsized condition due to reserve buoyancy provided by solid the boxes.

The concept of unsinkable small fishing boat was developed to the small passenger boats.

The application of light solid boxes was introduced to the passenger boat. However, early study was fail due to insufficient light solid boxes provided on board. The study was continued by applying air bags on board. The computation of required volume of combination of solid boxes and air bags was made. In fact, the total volume required including inner light solid boxes and air bags including parts of passenger body. This volume was added with outside air bags (side floaters) to support buoyancy force and to improve the stability of boat in flooding condition.

A boat model was developed and tested at small tank. The purpose of model test was to verify the required solid boxes and air bags as determined in theoretical computation (Hetharia, 2019). The result of the test confirmed the required amount of solid boxes and air bags to keep the model afloat. In addition, a full-scale boat was built (hull material of Fibreglass Reinforced Plastic /FRP) and tested at sea. The purpose of the test was to confirm the results of computation at the sea. The full-scale boat was provided with light solid boxes, on board air bags, the system to inflate air bags on board and outside air bags (side floaters). The side floaters contribute to support additional buoyancy and righting moment in flooding condition. During the sea trial, fifteen passengers and equipment was placed on board and the water was filled into the boat. The results of sea trial proved that the boat still floats. In addition, the boat was quite stable due to the contribution of side floater.

Basic principal of a ship to be float is the weight displacement of the ship equals to the total weight of ship (Barras, 2006; Biran, 2003; Moore, 2010). This is showed in the equation (1) as follows:

$$D = W \quad (1)$$

where:

D = Weight displacement

W = Total boat weight

The total boat weight consists of lightweight (LWT) and deadweight (DWT) (Parsons, 2003; Watson, 1998; Lewis, 1988) and is represented by:

$$W = LWT + DWT \quad (2)$$

The component of LWT consists of boat weight, propulsion system and equipment. The component of DWT consists of passengers and boat operator, luggage and fuel. Weight displacement of the boat (Δ) is computed as:

$$\Delta = C_B \times L \times B \times T \times \rho \quad (3)$$

where:

L = ship length B = ship beam

T = ship draft C_B = block coefficient

Δ = specific weight (1.025 ton/m^3, salt water)Therefore, for a ship to be float at the draft (T), then the total boat weight (W) equals to weight displacement (Δ).

In the case of a ship to be float or sink at ship height (H):

$$W_{total} > \Delta = C_B \times L \times B \times H \times \rho sink \quad (4)$$

$$W_{total} < \Delta = C_B \times L \times B \times H \times \rho float \quad (5)$$

During the boat operation the component of LWT is constant. The additional DWT component is coming from the water from outside the boat.

To reduce the incoming sea water on board, some materials should be provided. This concept is further explained with the help of Figure 1. The volume inside the boat consists of

boat structures (red colour) and solid boxes (blue colour), which are used as passenger seats. In fact, there is still inside volume may be filled with sea water (yellow colour). To prevent incoming water on board some amount of air bags (green colour) should be provided on board. However, the boat may still sink because of the limitation of air bags. The limitation of air bags correlate to the spaces required for the passengers.

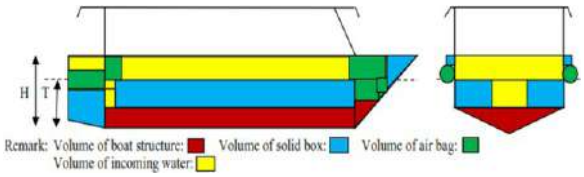

Figure 1. Composition of solid boxes and air bags

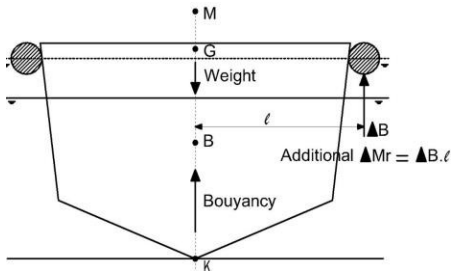

Figure 2. Contribution of side floater

Additional air bags should be provided at the outside boat or side floaters (green colour). The application of side floaters will increase the buoyancy and stability performance of the boat. Figure 2 shows the additional buoyancy force (▲B) and righting moment:

$$\blacktriangle Mr = \blacktriangle B \times l \qquad (6)$$

The volume of boat structures is composed on frames and sheets of material Fibre Reinforced Plastic (FRP). This volume acts as double bottom and double skin of the boat. Other solid boxes are closed spaces fixed at the bow and stern of the boat. The air bags are formed from expanded bags installed on board and outsides the boat. The bags are connected to two units of compressed air tank installed inside passenger seats. The air bags are stored in small boxes on board and outside the boat

METHODOLOGY

Collecting Boat Data and design Process

The existing boat data were collected in order to be used as input of re-design process. The boat data were collected at three local ports in Ambon Island. In this case the boat dimension and configuration are similar to the existing boat. The differences in re-design process are addressed to the application of light solid boxes, inside air bags and side floaters. Before developing a full-scale boat, a model was developed and tested to verify theoretical computation. A scale factor, λ = length of full-scale boat/length of model = 4 was determined. Dimensions of model and full-scale boat are presented at Table 1.

Table 1. The Dimensions of Boat and Model

No	Boat Parameters	Boat	Model	Unit
1	Length Overall, L_{OA}	6.61	1.652	m
2	Length of waterline, L_{WL}	6.35	1.587	m
3	Beam, B	1.40	0.350	m
4	Draft, T	0.40	0.100	m
5	Height, H	0.65	0.163	m
6	Speed, V	13.0	-	knot

Other boat data are described as follows :

Passenger : 14 persons
Operator : 1 person
Hull Material : FRP
Luggage : @ 20 kg for each passenger
Prime mover : 40 HP (outboard)
Equipment : anchor, rope, fuel tank

Developing Boat Drawings

The lines plan was developed by using the software Maxsurf in order to get boat parame-

ters. In addition, the lines plan, together with general arrangement, will be used to develop the model and full-scale boat. The computation of boat weight and the volume required for inner solid boxes and side floaters will be verified at the real model and full-scale boat. The lines plan and general arrangement are presented in Figures 3 and 4.

Developing and Testing the Model

The boat model was constructed in three phases namely inner template, model template and the model. The solid boxes and equipment were attached during the construction phase. The configuration of the model consist of hull model, inside solid boxes and air bags, passenger model, equipment.

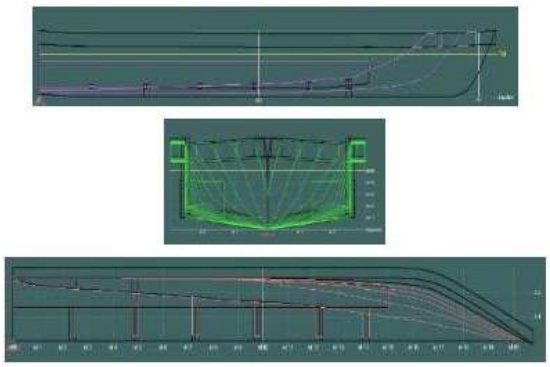

Figure 3. The lines plan

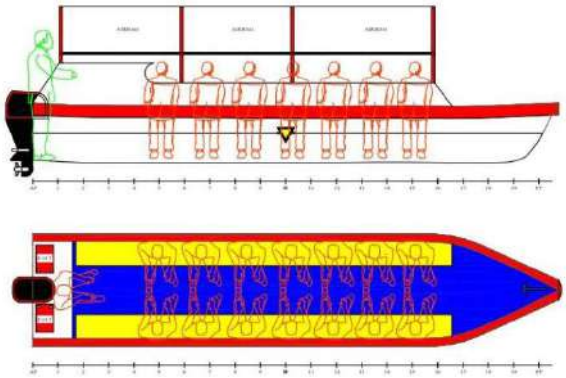

Figure 4. The general arrangement of boat

In addition, the side floaters were attached outside the boat (figure 5). The boat was filled fully with incoming water. Result of the test showed that with all configurations of solid boxes and air bags the model afloat. However, if the side floaters were removed then the model was sinking and capsized.

Figure 5. Model test

Developing and Testing the Full-scale Boat

The full-scale boat was tested to confirm the result of theoretical computation to the real condition at sea. The boat was developed in several phase, namely drawing the lines plan on the mould loft, cutting and developing the frames, developing the parent boat template, developing the boat template and constructing the full-scale boat (Figure 6). The propulsion and mechanical system was installed at the boat. The mechanical system consists of two air compressed tanks (attached under passenger seats), connecting system (hose and valves) and plastic bags. The compressed tanks supply the air into the plastic bags inside and outside the boat. The plastic bags were expanded when the boat is in critical condition (figure 7). The solid boxes installed on board consist on the passenger seat and additional boxes fitted at the bow and stern on board.

Figure 6. Full-scale unsinkable boat

Boat launching and sea trial was executed at sea. Test unsinkable boat was executed for two conditions which are without passengers and with passengers as seen in Figure 7.

Figure 7. Sea trial of unsinkable boat

RESULTS AND DISCUSSIONS

Results

The results of computations of boat volume are presented in Table 2. The boat components include the weight and volume of boat, solid boxes and air bags. In addition, the scenario of solid boxes and air bags based on their configuration is presented. Six scenarios were performed in order to find the configuration of solid boxes and air bags to prevent the boat from sinking. The first scenario was presented for the boat was at the designed draft due to normal loading condition.

At scenario 2, the boat was provided with solid boxes and loaded with passengers and incoming water. The result was the boat was sinking due to greater total boat weight. Similar way to scenario 2, at scenario 3 was added with inside air bags but it can't avoid the boat from sinking. At scenario 4 to 6, the boat was provided with outside air bags (side floaters). In this scenario, the dimension of side floater was varied to reach the configuration to support the boat from sinking and capsizing. The configuration of solid boxes and air bags that installed on board consists of:

- The volume of solid boxes : 1.213 m^3
- The volume of inside air bags : 0.511 m^3
- The volume of side floaters : 0.357 m^3

(Third scenario)

Table 2: Weight components of full-scale boat

No	Boat Parameters	Value	Unit
A	**Loaded to designed waterline (T = 0.4 m)**		
	Scenario 1: Boat + solid boxes + passengers		
1	Boat weight	2.284	ton
2	Volume displacement	2.236	m^3
3	Weight displacement	2.292	Ton
	Testing Result: the boat floats at designed draft		
B	**Loaded to boat height (H = 0.65 m)**		
4	Volume displacement boat	3.612	m^3
5	Volume displacement fender	0,147	m^3
6	Volume displacement boat & fender	3.760	dm^3
7	Weight displacement boat & fender	3.853	ton
	Scenario 2: Boat + solid boxes + passengers + water		
8	Boat weight	2.284	ton
9	Weight of water on board	2.385	ton
10	Total weight boat + water	4.668	ton
11	Weight displacement	3.853	ton
12	Weight displacement – total weight	-0.816	ton
	Testing Result: the boat sinks		
	Scenario 3: B + SB + AB + P + W		
13	Boat weight	2.284	ton
14	Weight of water on board	1.920	ton
15	Total weight boat + water	4.204	ton
16	Weight displacement	3.853	ton
17	Weight displacement – total weight	-0.351	ton
	Testing Result: boat sinks		
	Scenario 4: B + SB + AB + SF 1 + P + W		
18	Boat weight	2.284	ton
19	Weight of water on board	1.92	ton
20	Total weight boat + water + floater 1	4.239	ton
21	Weight displacement	3.942	ton
22	Weight displacement – total weight	-0.297	ton
	Testing Result: Model sinks		
	Scenario 5: B + SB + AB + SF 2 + P + W		
23	Boat weight	2.284	ton
24	Weight of water on board	1.920	ton
25	Total weight boat + water + floater 2	4.249	ton
26	Weight displacement	4.053	ton
27	Weight displacement – total weight	-0.195	ton
	Testing Result: Boat sinks		
	Scenario 6: B + SB + AB + SF 3 + P + W		
28	Boat weight	2.284	ton
29	Weight of water on board	1.920	ton
30	Total weight boat + water + floater 3	4.259	ton
31	Weight displacement	5.025	ton
32	Weight displacement – total weight	0.766	ton
	Testing Result: Boat floats		

Note:

B = boat, SB = Solid boxes, P = Passenger,

AB = Inside air bags, SF = Side floater,

W = Incoming water

Discussions

The results in Table 2 show the scenario on which configuration the boat will float or sink. To ensure the boat still float then the weight displacement of the boat should be greater than the total boat weight which includes the boat, passengers and incoming water. It is clearly seen that in the scenario number 2 to 5 the boat sinks. In fact, this condition occurs when the total boat weight exceed the displacement weight which come from buoyancy force. At the scenario number 6, the weight displacement was greater than total boat weight. This condition makes the boat floats. Furthermore, a small righting moment created by side floater contributes to balance the boat from heeling and capsizing. The righting moment comes from this approach :

- The volume of one side floater : 0.179 m3
- The weight displacement : 0.183 tons
- The distance from midship : 0.900 m
- The righting moment : 0.165 ton.m

CONCLUSION AND RECOMMENDATION

The study concerning the unsinkable small passenger boat have been end-up with a good selection of configurations of solid boxes and air bags. It may be resumed from the result of study that:

- Selection a proper configuration of solid boxes and air bags will provide the buoyancy and righting moment to prevent the boat from sinking and capsizing.
- The solid boxes and air bags installed on board contribute to reduce the incoming

water while the air bags outside the boat (side floaters) contribute to provide additional buoyancy and righting moment.

- To prevent the boat from sinking, it requires the volume of solid boxes 1.213 m^3 and air bags 0.511 m^3 inside the boat and side floaters (outside air bags) of 0.357 m^3.
- The total weight of boat, passengers and incoming water of 4.259 ton are ballanced by 5.025 weight displacement. In this condition, there are the amounts of reserve buoyancy of 0.766 ton. This reserve buoyancy contributes to float the boat under flooding condition.

It is recommended that additional solid boxes should be fitted at the bow and stern instead of solid boxes for the passenger seat as used by the existing boats. Additional inside air bags and side floaters may be used as reference to be installed on unsinkable boat. The results of study should be considered by the authority boards for future application for the existing small passenger boats.

ACKNOWLEDGEMENTS

Special thank is given to The Ministry of Research, Technology and Higher Education, The Republic of Indonesia for the research grant of "Penelitian Terapan Unggulan Perguruan Tinggi" 2018 - 2019 to execute this research

REFERENCES

Anonymous,(2026), "Data Kecelakaan Kapal Laut, BASARNAS Ambon".

Barras, B. and Derret, D. R. (2006), *Ship Stability for Masters and Mates*, Butterworth – Heinemann, 6th edition, An Imprint of Elsevier Ltd., Linacre House, Jordan Hill, Oxford OX2 8DP.

Biran, A. B. (2003), *Ship Hysrostatics and Stability*, Technion – Faculty of Mechanical Engineering, 1st publication, Butterworth – Heinemann, An Imprint of Elsevier Ltd., Linacre House, Jordan Hill, Oxford OX2 8DP.

Lewis, E. V. (1988), *Principles of Naval Architecture, Stability and Strength*, SNAME Publication, Vol. I, Jersey City, New Jersey.

Hetharia, W. R., and de Lima, E. J (2008), "Design and Evaluating of Unsinkable Tuna Long Boats", Proceeding of The 6th Regional Conference on Marine Technology (MARTEC 2008), University of Indonesia, Jakarta 26 – 27 August, 2008.

Hetharia, W. R., de Fretes, E. R., Gaspersz, , F., and Tianotak, A. J. (2014), "Kajian Tentang Beberapa Aktifitas Masyarakat Maluku di Sektor Kelautan", Prosiding Kongres Budaya Maluku, Ambon.

Hetharia, W. R. (2017), "Design and Application of Unsinkable Tuna Longboat for Local Fishermen", OCCASIONAL PAPERS No. 58 (March 2017),

Kagoshima University, Japan, 2017 www.http://cpi.kagoshima-u.ac.jp/index-j.html

Hetharia, W. R., Gaspersz, and F, Feninlambir, A. (2018), "Evaluasi Parameter Stabilitas Kapal Penumpang Kecil", Prosiding Seminar Nasional Fakultas Teknik Universitas Pattimura Ambon, 26 April 2018, ISSN : 2620-3995.

Hetharia W. R., de Fretes, E. R., Gaspersz, F., and Louhenapessy, Y. (2018), "The Application of Solid Box on Small Passenger Boat", Proceedings of International Conference on Marine Science and Technology – Sustainable Development on Marine Resources", Pattimura University Ambon, 24-25 October 2018, Ambon

https://www.researchgate.net/publication/336 866871 The application of solid box es on small passenger speed-boat

Hetharia W. R., de Fretes, E. R., Gaspersz, F., and Louhenapessy, Y. (2019), "A Model Scale of Unsinkable Small Passenger Speed-Boat", Proceedings of International Conference on Ship and Offshore Technology, Vol 2, Undip 25-26 November 2019, Semarang https://www.dropbox.com/s/ogiuq3nbg6y-tud2/ Porseeding%20Univ.Diponegoro.pdf?dl=0

Moore, C. S. (2010), *Intact Stability – The Principles of Naval Architecture Series*, The Society of Naval Architects, SNAME, Jersey City, New Jersey, 2010.

Parsons, M. G. (2003), *Parametric Design - Ship Design and Construction,* Chapter 11, Volume. 2., SNAME Publication, Jersey City, NJ, USA.

Watson, D. G. M (1998), *Practical Ship Design*, Elsevier Ocean Engineering Book Series, Volume

GNSS METEOROLOGY AND LAND SUBSIDENCE OF HEAVY RAINFALL IN JAKARTA ON JANUARY 1, 2020

Syachrul Arief[1], Mokhamad Nur Cahyadi[2]
Geospatial Information Agency Indonesia[1]
Dept. Geomatic Engineering, Institut Teknologi Sepuluh Nopember (ITS)[2]
e-mail : syachrul.arief@big.go.id

ABSTRACT

This study aims to demonstrate that GNSS meteorology can be applied in Indonesia, by estimating the zenith troposphere delay (ZTD) of sustainable GNSS stations in Indonesia, using one of the "goGPS" software packages. As a calculation with rain conditions, the ZTD value was converted into precipitation water vapor (PWV). This research is using GNSS meteorology to be applied into heavy rains at the end of 2019 in Jakarta which was hit by floods on December 31, 2019. According to a report by Geophysical Meteorology and Climatology Agency (BMKG), the main cause of this flood is a high rainfall. The rainfall gauge at Halim Perdanakusuma Station showed 377 mm of rainfall that day. Rain gauges at Taman Mini and Jatiasih stations record rainfall of 335 mm/day and 260 mm / day, respectively. From the GNSS data processing, the PWV values at the five GNSS stations show a similar pattern even though the average between stations is ~ 30 km. The PWV value appeared to be increased at noon on December 30, 2019, and the peak occurs at the end of the day on December 31, 2019. The PWV value showed a sudden drop at midday on January 1, 2020. In the end, the PWV increased again, but not as high as the first peak. From 2 January 2020, the PWV has decreased and has been maintained almost constantly until 4 January. Within this time frame, there were two peak PWV events. The PWV of the first peak was ~ 70 mm and the second peak was ~ 65 mm, and the largest peak PWV was recorded at the CJKT station.

Keywords : *GNSS, troposphere, PWV, heavy rain*

1. INTRODUCTION

In GNSS data analysis to obtain tropospheric parameters and station positions of the study of GNSS meteorology, Arief and Heki (2020), has downloaded the data from appropriate data sets available from various research centers, such as UNR and GSI. Arief and Heki (2020), studies were performed for heavy rain episodes in the Japan area where a large number of GNSS stations are available. This study analyzed the GNSS data taken in Indonesia and estimating tropospheric parameters as well as station positions using an alternative way, such as analyzing the data using an appropriate GNSS software package.UNAVCO(https://www.unavco.org/software/dataprocessing/postprocessing/postprocessing.html) stated that there are 3 distributions of GNSS software based on their use: "Research-Level", "Open-Source" and "Commercial". The usage of Open-Source software in Indonesia is quite promising and will develop rapidly in the future, considering that it is easy to obtain and simple to operate in order to get results. The concept of ground-based GNSS meteorology was proposed initially by Bevis et al. (1992). Nowadays, GNSS meteorology has become one of the essential means to observe precipitable water vapor (PWV), and PWV data from GEONET have been assimilated in the mesoscale model

of JMA to improve weather forecast accuracy since 2009 (e.g. Shoji, 2015).

Miyazaki et al. (2003) focused on such atmospheric delay gradients and showed that the temporal and spatial variations of the gradients were compatible with the humidity fields derived from ZWD and with the meteorological conditions in 1996 summer over the Japanese Islands (especially during a front passage). Shoji (2013) and Brenot et al. (2013) demonstrated the important role of the atmospheric delay gradients to detect small-scale structures of the troposphere than ZWD.

Recently, Zus et al. (2019) have successfully processed the Central Europe GNSS network data to show that the interpolation of ZWD observed with a sparse network can be improved by utilizing tropospheric delay gradients. They showed significant accuracy improvement for the simulation of the numerical weather model, and for the agreement of the simulation results with real observations, relative to the cases without utilizing tropospheric delay gradients.

The purpose of this study is to show that GNSS meteorology can be applied in Indonesia with a limited number of GNSS Networks, unlike in Japan, where the GNSS network is very large (Arief and Heki 2020). GNSS meteorology was calculated by estimating the peak tropospheric delay (ZTD) of continuous GNSS stations in Indonesia, using one of the "goGPS" software packages. In this study, GNSS meteorology was applied to the heavy rain events in early 2020 in Jakarta to analyze the correlation between rainfall and the land subsidence in the heavy rainfall area. Jakarta suffered from a flood on January 1, 2020.

According to a report from the Indonesian Meteorology and Climatology Geophysics Agency (BMKG), the main cause of this flood was a heavy rainfall. The rain gauge at the Halim Perdanakusuma station showed the rainfall of 377 mm on that day. The rain gauge at the station Taman Mini and Jatiasih recorded rain amounting to 335 mm/day and 260 mm/day, respectively. This rainfall distribution covered a large area and was quite high in value as shown in Figure.1

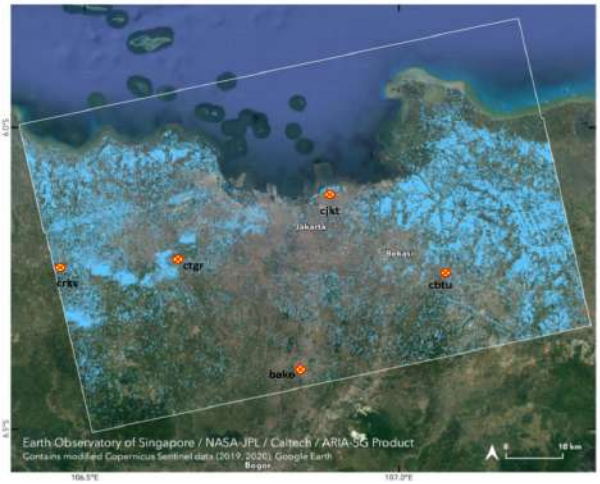

Figure 1. Figure.1, Map of the areas in Greater Jakarta showed the likely flooded areas (light blue pixels), based on synthetic aperture radar satellite data before (21 December 2019) and during (02 January 2020) the flood event. Based on the web page https://earthobservatory.nasa.gov/images/146113/torrential-rains-flood-indonesia

2. DATA AND METHODS

2.1 GNNS data set

The primary format of the GNSS data used in this study is the Receiver Independent Exchange (RINEX) format. Next, RINEX files was processed to estimate tropospheric parameters using sophisticated open-source GNSS software, called goGPS, version 1.0 Beta, from Geomatics Research and Development s.r.l. - Lomazzo, Italy (Realini, 2009). In the flood area, there were at least 5 GNSS stations has been identified and managed by BIG in the INACORS network. The 5 stations include CJKT in Jakarta, BAKO in Bogor, CBTU in Cibitung, CRKS in Cirakas, and CTGR in Tangerang. GNSS data was

obtained on the INACORS network using RINEX format. The data was used over 7 days, from 29th December 2019 to 4th January 2020 to obtain the phenomenon including the changes in several days before and after the flood and heavy rain.

The wet tropospheric delays were converted to PWV (Perceptible Water Vapor) in every 30 seconds. Large PWV brings intensive rainfall, and the record-making rainfall data from BMKG on 1 January 2020 have been associated with high PWV values. The vertical crustal movements have been analyzed as well using coordinates obtained by analyzing the RINEX data of goGPS software.

2.2 Software goGPS

The leading software for processing RINEX data, goGPS. (Realini, 2009), is an open-source software initially developed by Dr. E. Realini (with contributions from the various thesis works by master students) since 2007 at the Geomatics Laboratory of Politecnico in Milano, Como Campus. It is specifically designed to improve the positioning accuracy of low-cost GNSS devices by relative positioning and the Kalman filtering technique. goGPS code was published online as free and open-source software in 2009. The project is open to collaborations since its publication, and it has received supports and code contributions from users working in both academy and business companies in different countries (including Italy, Japan, Switzerland, Spain, and Germany).

Strategies for processing RINEX data with goGPS are as shown below

	goGPS 1.0 Beta
Strategy	Constellation: multi GNSS Processing technique: precise point positioning (PPP) Elevation cut-off angle: 7° Data processed in two 24 h sessions (from 00:00 to 24:00 UTC and from 12:00 UTC on day *D* to 12:00 UTC on day *D*+1) Frequency: L1, L2
Orbits and clocks	Fixed to JPL final orbits and clocks
Observation rate	30s sampling rate
Observation weighting	Uniform - all observations equally weighted
Tropospheric modeling	Niel Mapping Function Macmillan Mapping function for gradients A-priori zenith delay - VMF gridded zenith delays Meteorological data - Standard Atmosphere
Tropospheric estimates	One ZWD per 30 seconds, One tropospheric gradient per 30 seconds

2.3. Land Subsidence in Jakarta

Secular land subsidence in Jakarta, due to urbanization, has been studied over a long time. For example, Andreas et al. (2019) showed that Jakarta, compared with major cities on the coast of other countries, occupies the first position in terms of land subsidence from 1920 until now (Figure.2). Jakarta is vulnerable to further land subsidence, especially when heavy rain occurs and rainwater pools to cause a flood.

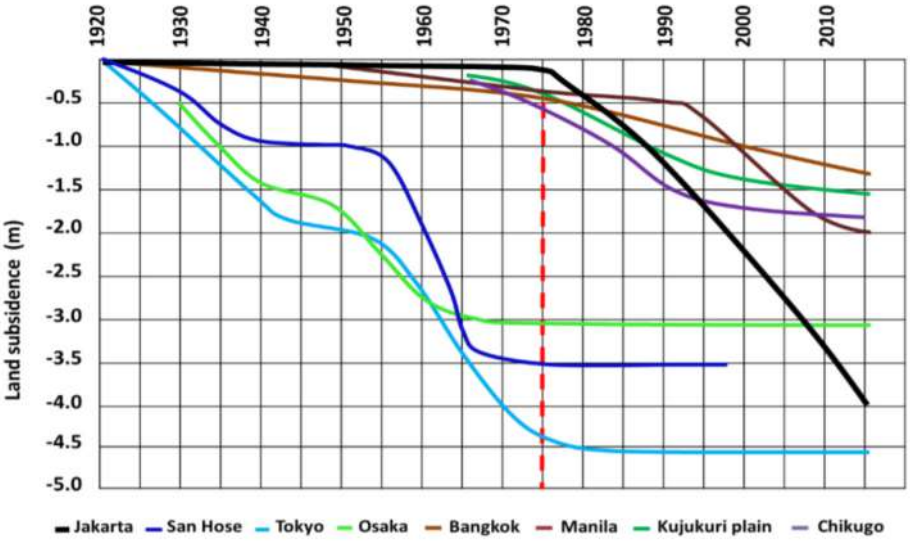

Figure 2, Land subsidence in several coastal cities in different countries including Jakarta, Indonesia, from 1920 until recent years (Andreas et al., 2019).

This study discussed the temporary land subsidence related to the occurrence of heavy rain on January 1, 2020, using the GNSS data analyzed with the open-source software goGPS. When heavy rain occurs, the water will gather at the surface of the land. This makes water loads to depress the ground surface and make it subside.

3. RESULT AND DISCUSSIONS

3.1. Determination of PWV values at 5 INACORS stations.

This study analyzed the crustal movements for the recent heavy rainfall event in Indonesia on January 1, 2020. This rain caused severe flooding around the Jakarta area and would be an appropriate case to study crustal deformation by surface rainwater load.

RINEX data obtained from the INACORS-BIG network has been analyzed using the goGPS open-source software package, as explained in subsection 2.2. Before studying crustal deformation, the ZTD value was estimated, and then it was isolated and converted into PWV. Figure.3 shows the result of the PWV time series at five INACORS stations evenly distributed within the flooded area on January 1, 2020.

Figure 3 Time series of PWV values at 5 INACORS GNSS stations in the Jakarta flood area. The time spans from 29 December 2019 to 4 January 2020 (UT), and the highest PWV value occurred on December 31, 2019

As seen in Figure. 3, the PWV values at the five GNSS stations show similar patterns despite the average inter-station of ~30km. PWV values appear to increase in the middle of the day of 30 December 2019, and the peak occurred at the end of the day of 31 December 2019. This condition is consistent with the date of heavy rain as discussed in Section 6.2.

The PWV value showed a sudden drop in the middle of the day 1 January 2020. At the end of the day, PWV increased again, but not as high as the first peak. From January 2, 2020, PWV decreased and kept nearly constant until January 4. In this time range, there were two peak PWV occurrences. The first peak PWV of ~70 mm and the second peak of ~65 mm, and the largest PWV were recorded at the CJKT station. Next, the rainfall events on 31 December 2019 were analyzed using data from JAXA Global Rainfall Watch, which offers hourly rainfall data. Figure.4 shows the hourly rainfall in Jakarta and surrounding areas obtained from this data set. The increase in rainfall starts at 07.00 (UT) until the peak at 10:00 (UT). Next, this information was compared with the hourly PWV values at GNSS stations shown in Figure. 5.

As seen by comparing Figure.4 and Figure.5, the rainfall and PWV time series show consistent behaviors. This explains that the heavy rain peak occurs when the PWV value is at its peak. It also indicates that the heavy rain caused a sudden drop of PWV from 10:00 to 12:00, which means that water vapor changed into liquid water (heavy rain). This suggests that monitoring the GNSS-meteorology data from INACORS is useful as a meteorological observation.

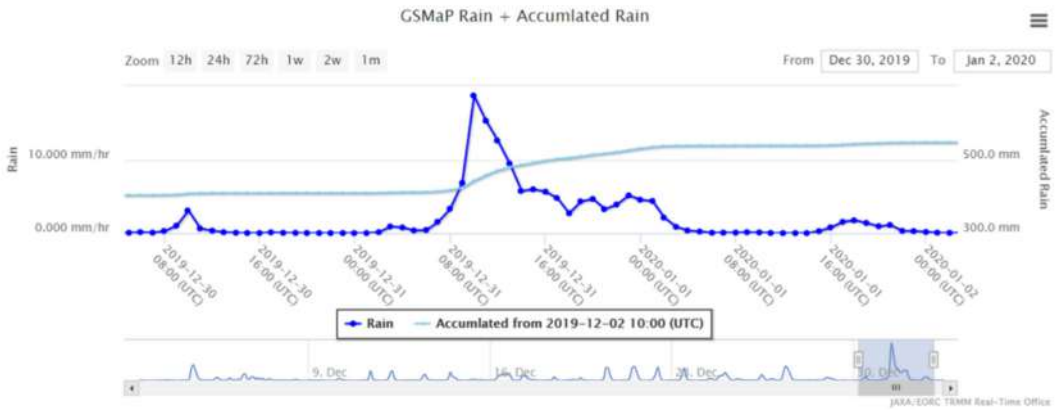

Figure 4. Rain rate and cumulative rain on December 31, 2019, according to the hourly rainfall data set from JAXA Global Rainfall Watch. The highest rainfall peak occurred around 10.00 am (UT) on that day.

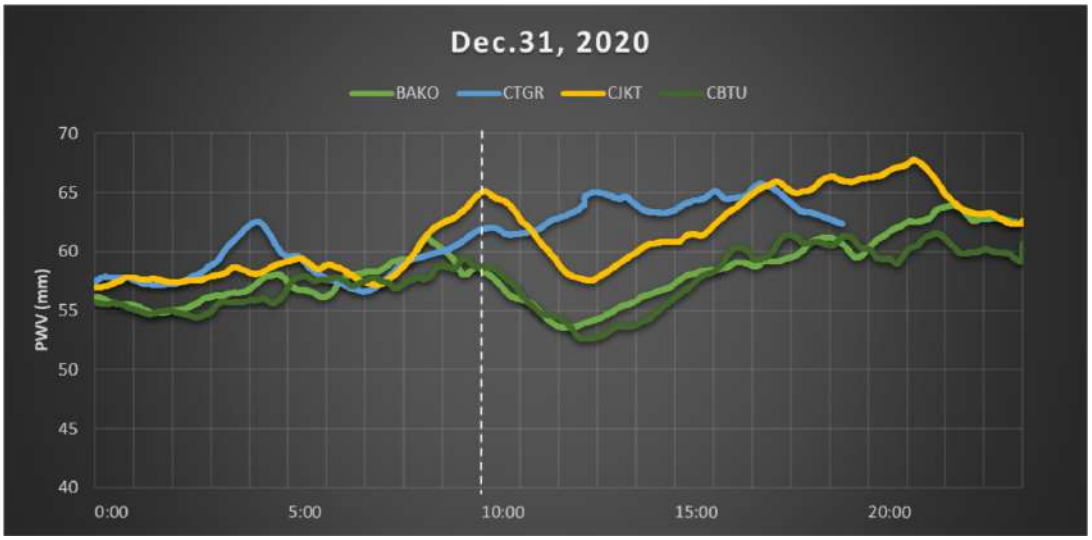

Figure 5. Hourly PWV values at 4 INACORS GNSS stations, BAKO, CTGR, CJKT, and CBTU stations during the day of December 31, 2019. PWV time series show maxima at 10.00, the peak rain rate time, at CJKT and BAKO stations.

3.2. Comparison of PWV INACORS with Jakarta Radiosonde Station

To compare the GNSS-PWV values with those by other sensors, the PWV data was obtained by radiosondes at BMKG, Jakarta. BMKG serves not only as of the GNSS stations but also as a radiosonde station in Jakarta with the name WIII station. Its primary purpose is to serve for flight at the Soekarno Hatta Airport, Cengkareng, Jakarta.

The radiosonde PWV data are compared with the PWV data obtained by an INACORS station in Jakarta CJKT as shown in Figure.6.

The correlation between the two PWV values is not so high, probably because of the distance between the two stations. Nevertheless, at least the PWV from GNSS stations can complement the radiosonde data with their high spatial and temporal resolution.

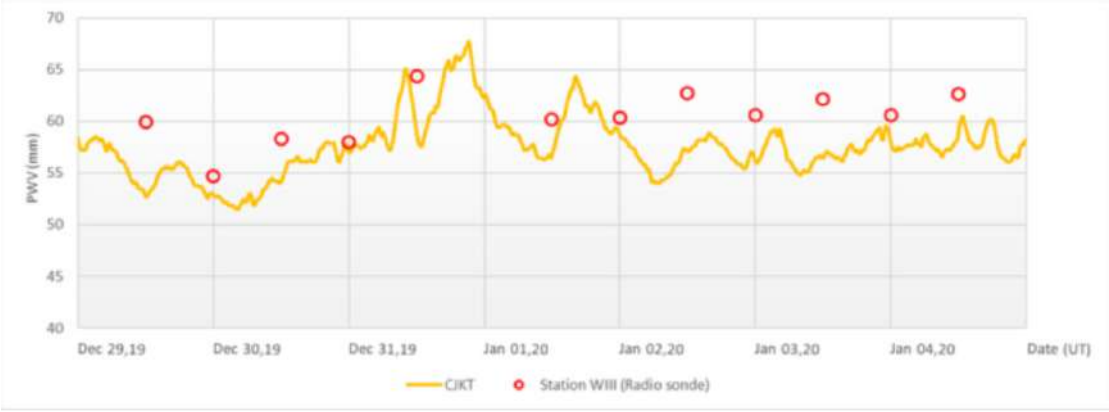

Figure 6. Comparison of PWV values between GNSS-PWV at CJKT stations estimated every 30 seconds (orange curve) and radiosonde-PWV recorded every 6 hours at the WIII station (red circle). The correlation coefficient between PWV data from GNSS and radiosond

3.3. Crustal movement analysis, GNSS station (INACORS-BIG)

Next, the hypothesis about temporary vertical movements of GNSS stations reflect has been tested to some extent of surface loads such as rainwater. The vertical positions of the GNSS stations have been estimated to study vertical crustal movements during the floods on January 1, 2020, and heavy rains on December 31, 2019. The vertical positions have been calculated during a period from 10 days before the flood (December 22-31 December 2019) to 9 days after the flood. (2-10 Jan 2020).

The GNSS data in RINEX format was used in this research, with supporting data for the satellite ephemeris. The software outputs topo centric coordinates, composed of north-south, east-west, and vertical movement components. The vertical movements are very interesting because the water load will depress the ground vertically. The vertical coordinate time series have been plotted in Figure 7.

From the 5 GNSS-INACORS stations located in the Jakarta flood area, data on 1 Jan 2020 from the BAKO station could not be processed because the data had experienced an interruption during the acquisition process.

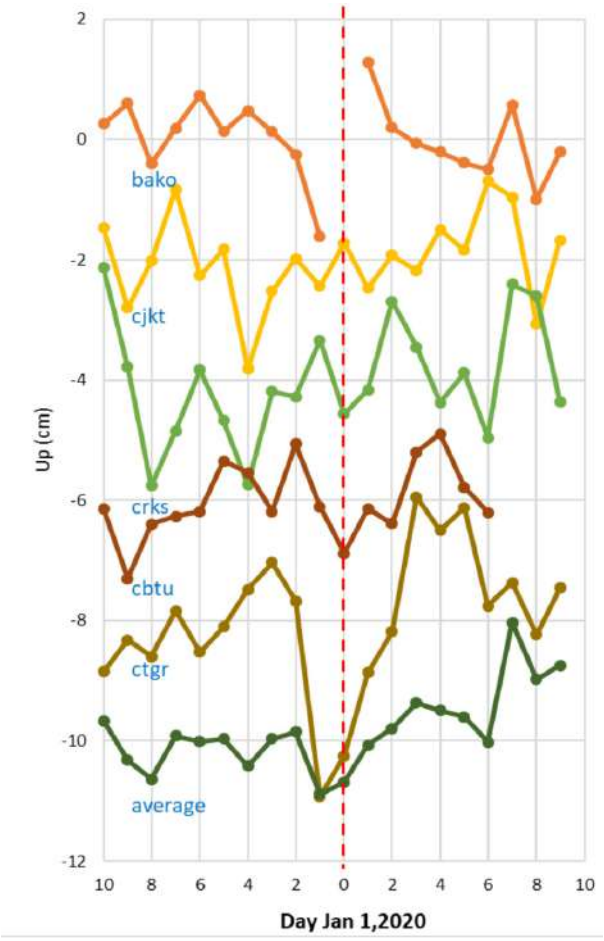

Figure 7, Vertical position time series over a period spanning 20 days for the 5 GNSS stations in the region flooded by the January 1st, 2020, Jakarta heavy rain. The station Bako had a data interruption on January 1, 2020.

Figure 7 shows that the average vertical coordinates show significant subsidence of nearly 1 cm on December 31, 2019, and January 1, 2020. However, coordinates of the individual stations behave differently. For example, subsidence on December 31, 2019, was seen only at BAKO and CTGR stations. Subsidence on January 1, 2020, was clear for the CRKS, CTGR, and CBTU stations. These stations were located in the flooded area (a light blue colored region in Figure 1). On the other hand, CJKT was close to the coast and not included in the flooded area. These results suggest that subsidence due to flood water load is quite non-uniform in space, and a dense network would be needed to fully understand the crustal response to the surface storm water load in Indonesia.

4. CONCLUSION

Using the method from goGPS, GNSS data was analyzed from INACORS, Indonesia's permanent GNSS network, to study tropospheric parameters and scale descent. In the first result, the PWV value was obtained from GNSS data from Jakarta when there was heavy rain on January 1, 2020. Then, the consistency was compared with the closest radiosonde observation results. This showed a suitable correlation between the PWV value although it is small since it has been influenced by the distance of GNSS and radiosonde stations.

Finally, the crust movement has been analyzed using goGPS method with similar GNSS data. The results showed vertical movements during heavy rain in Jakarta, namely all GNSS stations in the Jakarta area showed a significant change from December 31, 2019, to January 1, 2020. This shows that flooding in Jakarta caused temporary land subsidence. Therefore, further study is needed to compare other times or places with the occurrence of the same phenomenon.

REFERENCES

Andreas, H. et al (2019) IOP Conf. Ser.: Earth Environ. Sci. 389 012034

Arief, S., and Heki, K. (2020). GNSS Meteorology for Disastrous Rainfalls in 2017–2019 Summer in SW Japan: A New Approach Utilizing Atmospheric Delay Gradients. Front. Earth Sci. 8, DOI: 10.3389/feart.2020.00182.

Bevis, M, S Businger, T A Herring, C Rocken, R A Anthes, and R H Ware. 1992. "GPS Meteorology: Remote Sensing of Atmospheric Water Vapor Using the Global Positioning System." Journal of Geophysical Research.

Brenot, H., J. Neméghaire, L. Delobbe, N. Clerbaux, P. De Meutter, A. Deckmyn, A. Delcloo, L. Frappez, and M. Van Roozendael. 2013. "Preliminary Signs of the Initiation of Deep Convection by GNSS." Atmospheric Chemistry and Physics 13 (11): 5425–49. https://doi.org/10.5194/acp-13-5425-2013.

https://earthobservatory.nasa.gov/images/146113/torrential-rains-flood-indonesia, Map of the areas in Greater Jakarta showing the likely flooded areas (light blue pixels), based on synthetic aperture radar satellite data.

https://nasional.kompas.com/read/2020/01/03/10141971/bmkg-sebut-curah-hujan-di-jakarta-awal-2020-paling-ekstrem-dalam-sejarah.

https://sharaku.eorc.jaxa.jp/GSMaP/, JAXA Global Rainfall Watch, Rain rate and cumulative rain 2019-2020.

Miyazaki, Shin'ichi, Tetsuya Iwabuchi, Kosuke Heki, and Isao Naito. 2003. "An Impact of Estimating Tropospheric Delay Gradients on Precise Positioning in the Summer

Using the Japanese Nationwide GPS Array." Journal of Geophysical Research: Solid Earth 108 (B7). https://doi.org/10.1029/2000JB000113.

Realini, E. (2009). goGPS free and constrained relative kinematic positioning with low-cost receivers. Ph. D. thesis, http://www.researchgate.net/publication/237520116

Shoji, Yoshinori. 2013. "Retrieval of Water Vapor Inhomogeneity Using the Japanese Nationwide GPS Array and Its Potential for Prediction of Convective Precipitation." Journal of the Meteorological Society of Japan 91 (1): 43–62. https://doi.org/10.2151/jmsj.2013-103.

Shoji, Y., 2015. "Water vapor estimation using ground-based GNSS observation network and its application for meteorology." Tenki 62:3-19.

Zus, Florian, Jan Douša, Michal Kačmařík, Pavel Václavovic, Kyriakos Balidakis, Galina Dick, and Jens Wickert. 2019. "Improving GNSS Zenith Wet Delay Interpolation by Utilizing Tropospheric Gradients: Experiments with a Dense Station Network in Central Europe in the Warm Season." Remote Sensing 11 (6): 674. https://doi.org/10.3390/rs11060674.

COMPUTATIONAL ANALYSIS ON HEAVE AND PITCH MOTIONS PERFORMANCE OF A HYDROFOIL SHIP

A. Fitriadhy[1,*], N. Amira Adam[2], and M. Syafiq Zikry[3]

[1] Faculty of Ocean Engineering Technology and Informatics, Universiti Malaysia Terengganu, 21030 Kuala Terengganu, Terengganu, Malaysia

[2] Postgraduate Student, Faculty of Ocean Engineering Technology and Informatics, Universiti Malaysia Terengganu, 21030 Kuala Terengganu, Terengganu, Malaysia

[3] Undergraduate Student, Faculty of Ocean Engineering Technology and Informatics, Universiti Malaysia Terengganu, 21030 Kuala Terengganu, Terengganu, Malaysia

[*] E-mail : naoe.afit@gmail.com

ABSTRACT.

Hydrofoil ship usually experiences high resistance and excessive heave and pitch that may lead to downgrade her seakeeping performance. Therefore, a reliable investigation on prediction of a seakeeping performance of a hydrofoil ship in head-seas is obviously required. To achieve this objective, an analysis of Computational Fluid Dynamic (CFD) approach on hydrofoil ship motion is then proposed. Several parameters such as angle of stern foil and Froude Number have been accordingly taken into account in the simulation, where the fore foil angle is constantly 5°. In general, the results revealed that the increase of the stern foil angle was proportional to the heave motion of the hydrofoil ship. As compared to the magnitude of the stern foil angle of 5° and 10°, the heave motion of the hydrofoil ship has sufficiently decreased at the stern foil angle of 7.5°, which leads to have a better seakeeping performance. Furthermore, the subsequent increase of Froude number pointing towards reduction of heave motion, which was inversely proportional to the magnitude of her pitch motion. Inherently, these have led to degrade of the hydrofoil ship seakeeping performances presented in the form of high Response Amplitude Operators (RAO). In general, this CFD simulation is very beneficial to ensure an operational effectiveness of hydrofoil design in high sea states with respect to the aforementioned design parameter.

Keywords : *CFD, hydrofoil, angle of stern foil, heave, pitch*

1.0 Introduction

Basically, hydrofoil ship usually consists of a wing like structure mounted on struts below the hull called as foil. This foil provides vertical force to rise up the ship out of the water surface during sailing. Therefore, this foil structure plays an important role in the design of the hydrofoil ship to minimize the drag force as well as reducing the ship's draft and her wetted surface area. As a result, the hydrofoil ship has dealt with less fuel consumption and increased marine eligibility, Matveev and Duncan (2005),

As a common ship, a seakeeping performance of the hydrofoil ship is a very prominent aspect to be analyzed in the early design stage. Several researchers had studied on the ship seakeeping behavior via numerical and experimental approaches. Faltinsen (1971) and Ma et al. (2016) investigated on seakeeping analysis by using the theoretical method. This approach is very efficient and requires relatively small computer resources. However, this method requires a very large data base of ship characteristics. The problem of organizing such a data base becomes the main difficulty of applying the method. In addition, (Islam, Jahra, & Hiscock, 2016; Sun, Yao, Xiong, & Ye, 2017; Vakilabadi, Khedmati, & Seif, 2014; Yao, Sun, Wang, & Ye, 2017) have experimentally conducted model test at towing tank. Even so, the experimental method is a time-consuming, complex procedure process and costly; and even impractical for various seakeeping test configurations (Fitriadhy & Adam, 2017). Meanwhile, the accuracy of the typical numerical approach requires necessarily further verification since some simplified simulation conditions were assumed to be given. Whilst a Computational Fluid Dynamic (CFD) approach for assessing the seakeeping performance on the hydrofoil ship put very demanding requirements with regards to a more reliable result both of accuracy and precision. According to Vakilabadi et al. (2014), the seakeeping results of the tests are used to produce transfer functions for heave and pitch motions, where the non-dimensional are called Response Amplitude Operators (RAOs). The study from Fitriadhy, Razali, and Aqilah Mansor

(2017) and Fitriadhy and Adam (2017) found that the seakeeping quality of the ship has been improved by presented the sufficient reduction of the RAO. In addition, the fully submerged hydrofoil control system was applied to control her vertical motion, Kim and Yamato (2004) and Kim and Yamato (2005). Similarly, Bai and Kim (2010) employed various types of control algorithms, and found that PID controller reduced effectively the vertical motion of the hydrofoil ship in the absence of incident waves

This paper presents Computational Fluid Dyanmic (CFD) analysis on heave and pitch motions of a hydrofoil ship. Several parameters such as various angles of stern foil and Froude numbers have been taken into account. Commercial CFD software, namely Flow3D, was utilized by applying the incompressible unsteady Reynolds-Averaged Navier Stokes equations in which RANSE and continuity equations are discretized by the finite volume method based on Volume of Fluid (VOF) to deal with the non-linear free surface. In addition, the mesh generation, boundary condition, initial condition and numerical option were carefully determined before simulations. Basically, this simulation solved the mesh independent study to select the optimal domain discretization. The Response Amplitude Operator (RAO) of heave and pitch motion performances are then discussed.

2.0 Mathematical Equation

Basically, two equations in accordance with the law conservation of mass and momentum as clearly expressed in Eqs. (1)-(4). The current CFD simulation is based on the incompressible unsteady RANSE, which employs the volume of fluid (VOF).

2.1 Continuity and Momentum Equations

The general mass continuity equation is presented in Eq. (1), for a moving object and the comparative VOF function transport equation; where the V_F is the fractional volume open to flow, ρ is the fluid density, R_{DIF} is a turbulent diffusion term, R_{SOR} is a mass source and A_x, A_y and A_z is the fractional area open to flow in x, y and z-direction, respectively (Manual, 2011).

$$V_F\frac{\partial \rho}{\partial t}+\frac{\partial}{\partial x}(\rho u A_x)+R\frac{\partial}{\partial y}(\rho v A_y)+\frac{\partial}{\partial z}(\rho \omega A_z)+\xi\frac{\rho u A_x}{x}=R_{DIF}+R_{SOR} \quad (1)$$

The momentum theory also applies in three coordinates direction (u, v, w) that has been used in the motion equation as displayed in Eqs. (2)-(4).

$$\frac{\partial u}{\partial t}+\frac{1}{V_F}\left\{uA_x\frac{\partial u}{\partial x}+vA_yR\frac{\partial u}{\partial y}+uA_z\frac{\partial u}{\partial z}\right\}-\xi\frac{A_y v^2}{xV_F} = -\frac{1}{\rho}\frac{\partial p}{\partial x}+G_x+f_x-b_x-\frac{R_{SOR}}{\rho V_F}(u-u_w-\delta u_s) \quad (2)$$

$$\frac{\partial v}{\partial t}+\frac{1}{V_F}\left\{uA_x\frac{\partial v}{\partial x}+vA_yR\frac{\partial v}{\partial y}+uA_z\frac{\partial v}{\partial z}\right\}+\xi\frac{A_y uv}{xV_F} = -\frac{1}{\rho}(R)\frac{\partial p}{\partial y}+G_y+f_y-b_y-\frac{R_{SOR}}{\rho V_F}(v-v_w-\delta v_s) \quad (3)$$

$$\frac{\partial w}{\partial t}+\frac{1}{V_F}\left\{uA_x\frac{\partial w}{\partial x}+vA_yR\frac{\partial w}{\partial y}+uA_z\frac{\partial w}{\partial z}\right\}=-\frac{1}{\rho}\frac{\partial p}{\partial z}+G_z+f_z-b_z-\frac{R_{SOR}}{\rho V_F}(w-w_w-\delta w_s) \quad (4)$$

where (G_x, G_y, G_z) are body accelerations, (f_x, f_y, f_z) are viscous accelerations and (b_x, b_y, b_z) are flow losses in porous media or across porous baffle plates, and the final condition account for the injection of mass at a source represented by a geometry element (Manual, 2011).

2.2 Turbulence Model

In the current CFD simulation, Renormalization-group (RNG) turbulence model has been selected considering for low Reynolds number effects (Koutsourakis, Bartzis, & Markatos, 2012; A. Yakhot, Rakib, & Flannery, 1994; V. Yakhot & Orszag, 1986). Through applying the double averaging strategy to the transport equations for Turbulent Kinetic Energy (TKE) and its dissipation rate produces the turbulence model for the flow as displayed in Eqs. (5)-(8).

$$\frac{\delta k}{\delta t} + U_j \frac{\delta k}{\delta x_j} = \frac{\delta}{\delta x_j}\left[\left(v + \frac{v_t}{\sigma_k}\right)\frac{\delta k}{\delta x_j}\right] + P_k + B_k + W_k \quad (5)$$

$$\frac{\delta \varepsilon}{\delta t} + U_j \frac{\delta \varepsilon}{\delta x_j} = \frac{\delta}{\delta x_j}\left[\left(v + \frac{v_t}{\sigma_\varepsilon}\right)\frac{\delta \varepsilon}{\delta x_j}\right] + C_{1\varepsilon}\frac{\varepsilon}{k}(P_k + B_k)(1 + \quad C_{3\varepsilon}R_f) + W_\varepsilon - C^*_{2\varepsilon}\frac{\varepsilon^2}{k} \quad (6)$$

$$P_k = v_t S^2 = v_t\left(\frac{\delta U_i}{\delta x_j} + \frac{\delta U_j}{\delta x_i}\right)\frac{\delta U_i}{\delta x_j} \quad (7)$$

$$B_k = \beta g_i \frac{v_t}{\sigma_s}\frac{\delta s}{\delta x_i} \quad (8)$$

where P_k is the shear production term of TKE, $S = 2\overline{S_{ij}S_{ij}}$ is the average of strain tensor and $S_{ij} = \frac{1}{2}\left(\frac{\delta U_j}{\delta x_i} + \frac{\delta U_i}{\delta x_j}\right)$, B_k and W_k is the buoyant and wake production term of TKE, respectively. In addition, W_ε is the wake production term in ε, σ_k and σ_ε are the turbulent Prandtl numbers for k and ε, and $C_{i\varepsilon}$, $C_{3\varepsilon}$ and $C^*_{2\varepsilon}$ are model coefficients.

2.3 Heave and pitch motions

In these equations, M is the vessel mass, I_5 is the moment of inertia in pitch and A_{ih}, B_{ij}, and C_{ij} are coefficients of added mass, damping and restoring coefficient, respectively. Also, F_3 and F_5 are vertical force and longitudinal subverting moment on the vessel respectively (Seif, Mehdigholi, & Najafi, 2014).

The degree of freedom (D.O.F) represented the possible translations and rotation of the body. The heave and pitch motion noted as translation and rotation respectively along X, Y and Z axis that define the behaviour of the hydrofoil ship during sailing. Heave motion is the linear vertical upward and downward acceleration of ships along their vertical axis.

Besides, the pitch motion occurred at ship's motion lifted at the bow and lowered at the stern and vice versa. The equations are demonstrated as Eqs. 9 and 10.

$$(M + A_{33})\frac{d^2\eta_3}{dt_2} + B_{33}\frac{d\eta_3}{dt} + C_{33}\eta_3 + A_{35}\frac{d^2\eta_5}{dt_2} + B_{35}\frac{d\eta_5}{dt} + C_{35}\eta_{5=}F_3 \quad (9)$$

$$A_{53}\frac{d^2\eta_3}{dt_2} + B_{53}\frac{d\eta_3}{dt} + C_{53}\eta_3 + (I_{55} + A_{35})\frac{d^2\eta_5}{dt_2} + B_{35}\frac{d\eta_5}{dt} + C_{55}\eta_{=}F_5 \quad (10)$$

Table 1. Dimension of hydrofoil ship in full scale and model scale

Geometrical parameters	Full scale	Model scale
Length Overall, LOA (m)	32.64	16.32
Length Between Perpendicular, LBP (m)	32.276	16.138
Beam, B (m)	8.278	4.139
Draft, T (m)	1.4	0.7

3.0 Simulation Condition

3.1 Principle Data of Propeller

The 3D geometry of the hydrofoil ship is clearly shown in **Fig. 1**. The details of the ship are completely summarized in **Table 1**.

3.2 Parametric Studies

In the current CFD simulation, several parametric studies such as various angles of stern foil and Froude numbers have been taken into consideration. Here, the bow foil angle magnitude of 5° with constant regular wave condition has been employed. The detailed parameter are completely summarized in **Table 2**.

3.3 Computational Domain and Mesh Generation

The computational domain is presented as structured mesh that is defined in a Cartesian. Each of the boundary conditions as shown in the mesh block 1 and mesh block 2, is displayed in **Fig. 2 (left)**. Referring to mesh block 1, the boundary condition at X_{min} is defined as wave, while X_{max} is defined by outflow boundary to absorb the wave motion which will reduce the reflection from the boundary. Y_{min}, Y_{max} and Z_{min} are assigned as symmetry boundary which it applies zero-gradient condition at the boundary and Z_{max} using specified pressure to create a uniform pressure in the boundary. All mesh boundaries for mesh block 2 are defined by symmetry. The boundary conditions for the current CFD simulations are completely presented in **Table 3**.

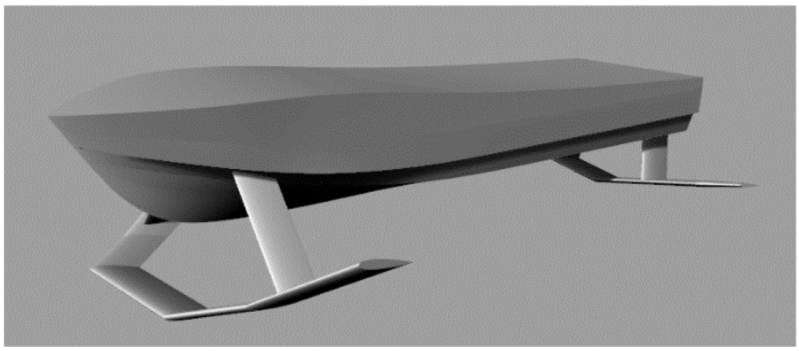

Figure 1. 3D model of a hydrofoil ship

Table 2. Matrix of computational simulation

Froude No.	Angle of stern foil (degree)		
	5	7.5	10
1.382	-	√	-
1.423	-	√	-
1.545	-	√	-
1.626	√	√	√
1.708	-	√	-
1.830	-	√	-

Referring to **Table 4**, four difference total number of cell meshing has been conducted to select an adequate number of cells meshing indicated by steadiness and computation time. In this research, the total number of cells meshing of 2,929,615 (case C) has been chosen to apply for all simulation. The increases of total number of cells meshing up to 3,536,935 (case D) was obviously unnecessary due to insignificant of percentage of difference.

Table 3. Boundary conditions

Boundary	Mesh block 1	Mesh block 2
Xmin	Wave	Symmetry
Xmax	Outflow	Symmetry
Ymin	Symmetry	Symmetry
Ymax	Symmetry	Symmetry
Zmin	Symmetry	Symmetry
Zmax	Specified Pressure	Symmetry

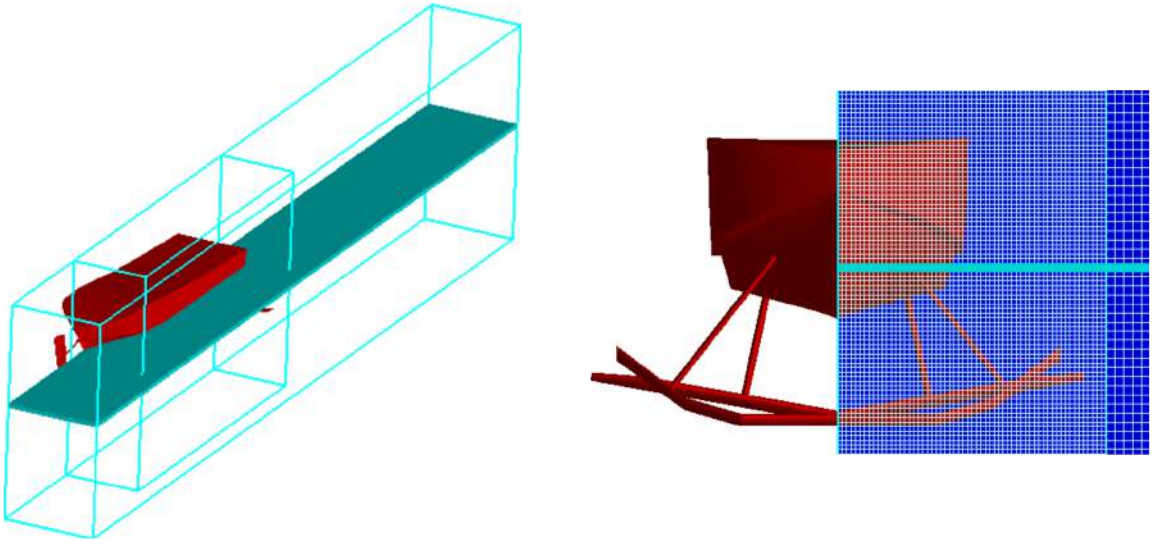

Figure 2. Overall mesh block using in simulation

Table 4. The mesh independent study on hydrofoil ship simulation

Case	Total number of cells	Time taken (hours)	Heave motion (m)
A	1,895,733	50	0.2867
B	2,246,994	62	0.2265
C	2,929,615	78	0.1692
D	3,536,935	96	0.1621

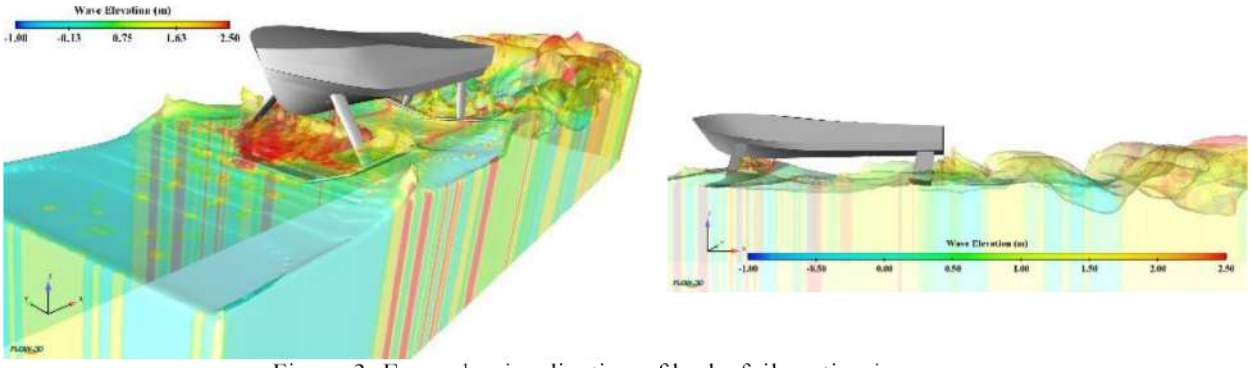

Figure 3. Example visualization of hydrofoil motion in waves

4.0 Results and Discussion

The CFD simulations have been carried out to predict the heave and pitch motions performance of hydrofoil at the various angles of stern foil and Froude numbers. The simulation results have been displayed and discussed in the **Sub-sections 4.1 ~ 4.2**.

***4.1** Effect of Foil's Angle at the Stern*

Referring to **Fig. 4**, the subsequent increase of angle of stern foil from 5° to 10° results in more significant influence to the heave and pitch motions of hydrofoils ship. It was noted that the heave motion remarkably increased up to 236.5% as the angle of stern foil increased from at 7.5° to 10°; meanwhile, her pitch motion was relatively steady. In addition, the pitch motion sufficiently decreased by 20.1% due to reduction of the stern foil angle of 5° to 7.5°. The

results are completely presented in **Table 4**. Based on the current results, it is merely concluded that the vertical motions behaviour at the stern foil angle of 7.5° coupled with bow foil angle of 5° provides a better seakeeping performance indicated with the less magnitude of heave and pitch motions (see **Fig. 5**) compared to the stern foil angle of 5° and 10°. However, the large magnitude of heave and pitch motions at the stern foil angles of 5° and 10° have potentially degraded the seakeeping performance of the hydrofoil ship due to precence of the unfavorable vertical ship motions. This non-linearity in the hydrofoil motions introduced by the waves coupled with the hydrodynamic effect of the stern foil, which demands a more comprehensive investigation in dealing with this complex problem. This is similar to what was reported by Keuning (1979) and Reguram, Surendran, and Lee (2016), where the angle of foil produced the significant influence of ship's responses.

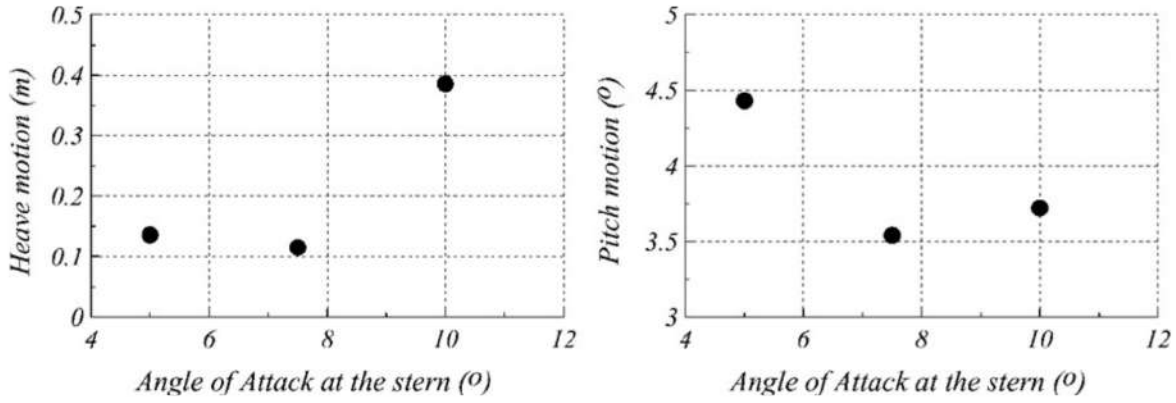

Figure 4. Heave (left) and pitch (right) motions characteristics at various angles of stern's foil, where the fore foil angle is 5°

Table 5. Heave and pitch motions charactersitics at various angle of stern foil

Angle of stern foil (◦)	Heave motion (m)	Pitch motion (◦)
5	0.1357	4.43
7.5	0.1147	3.54
10	0.3860	3.72

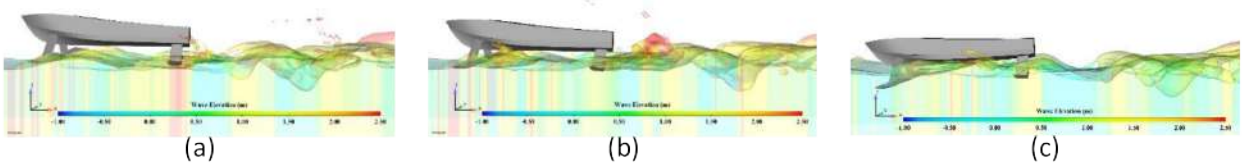

(a) (b) (c)

Figure 5. Vertical motion of hydrofoil characteristrics at various angle of stern foils (a) 5°, (b) 7.5° and (c) 10°, where the fore foil angle is 5° and Fr = 1.626

4.2 Effect of Various Froude Number (Fr) on Hydrofoil Ship

The heave and pitch motions of hydrofoil ship at various Froude numbers are displayed in **Fig. 6**, where the results are completely summarized in **Table 6**. The the hydrofoil ship at Fr = 1.382 showed a significant influence where it resulted in the higher heave motion as compared with the case of the other forward velocities. It was pointed out here that the further increase of the Froude number (Fr > 1.545), the hydrofoil ship has constituted a steady-state condition for her heave motion characteristics. The finding was reasonable since the hydrofoil ship configurations requires appropriate speed to generate lifting

forces and reduce the drag force between the wetted surface area and water surfaces (McCauley, 2018). In this condition, the hydrodynamics support allows the hydrofoil to remain an even keel condition and stable sailing with high positive dynamics pressure. This can be explained by the fact that the subsequent increase of Froude numbers led to decrease the drag, by lifting the hull out of water (see **Fig. 7**). Looking into a nonlinear trend of her sekaeeping behaviour in waves, the highest amplitude motic Adaofher heave and pitch motions at Fr = 1.382 were 0.5268 m and 5.5°, respectively. Th indicated that the seakeeping behaviour of tl hydrofoil ship gradually degraded, which can b explained by the fact that the hydrofoil ship ha more vigorous heave and pitch motions, whic was uncomfortable for the sailing (Keuning Van Walree, 2006

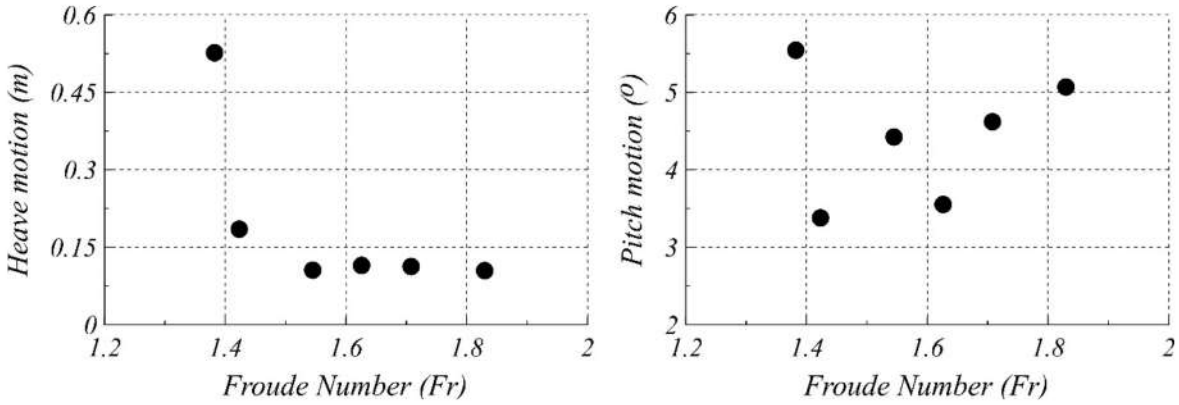

Figure 6. Heave (left) and pitch (right) motions of various Froude numbers

Table 6. Heave and pitch motions for various Froude numbers

Froude number	Heave motion (m)	Pitch motion (◦)
1.382	0.5268	5.5463
1.423	0.1851	3.3816
1.545	0.1060	4.4231
1.626	0.1147	3.5523
1.708	0.1129	4.6204
1.830	0.1048	5.0699

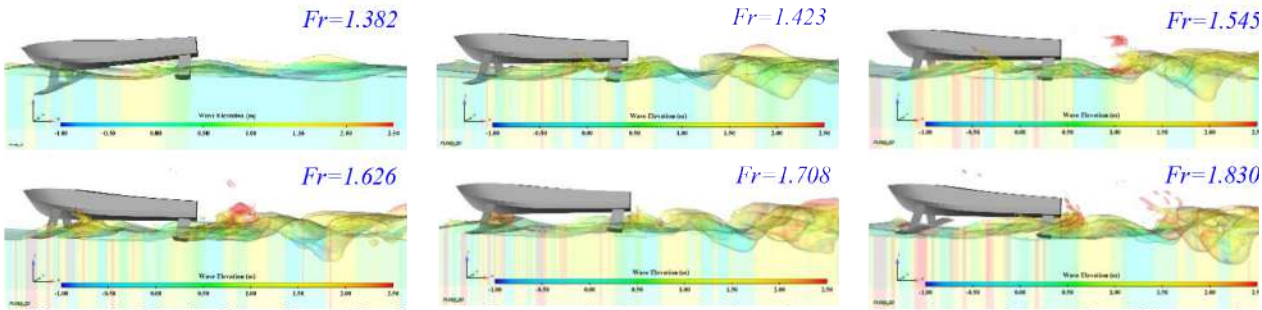

Figure 7. Vertical motion of hydrofoil characteristrics at various Froude numbers with angle of fore and stern foils are 5° and 7.5°, respectively

5.0 Conclusion

The simulation on predicting heave and pitch motions of the hydrofoil ship has successfully performed using the Computational Fluid Dynamic (CFD). The effect of the various angle of stern foil

and Froude numbers in regular wave condition. The results are as follow:

- Through employing the stern foil angle of 7.5° coupled with bow foil angle of 5°, the heave and pitch motions of the hydrofoil ship have sufficiently decreased, which may lead to provide a better seakeeping performance.
- The angle of stern foil has more significant effect to the seakeeping performances as compared to the effect of the forward velocities.

References

Bai, J., & Kim, Y. (2010). Control of the vertical motion of a hydrofoil vessel. *Ships and Offshore Structures, 5*(3), 189-198.

Faltinsen, O. (1971). *A rational strip theory of ship motions: Part II*. Retrieved from

Fitriadhy, A., & Adam, N. A. (2017). Heave and pitch motions performance of a monotricat ship in head-seas. *International Journal of Automotive and Mechanical Engineering, 14*, 4243-4258.

Fitriadhy, A., Razali, N., & Aqilah Mansor, N. (2017). Seakeeping performance of a rounded hull catamaran in waves using CFD approach. *Journal of Mechanical Engineering and Sciences, 11*(2), 2601-2614.

Islam, M., Jahra, F., & Hiscock, S. (2016). Data analysis methodologies for hydrodynamic experiments in waves. *Journal of Naval Architecture and Marine Engineering, 13*(1), 1-15.

Keuning, J. (1979). A calculation method for the heave and pitch motions of a hydrofoil boat in waves. *International Shipbuilding Progress, 26*(302).

Keuning, J., & Van Walree, F. (2006). *The comparison of the hydrodynamic behaviour of three fast patrol boats with special hull geometries.* Paper presented at the Proceedings of the 5th International Conference on High Performance Marine Vehicles.

Kim, S.-H., & Yamato, H. (2004). An experimental study of the longitudinal motion control of a fully submerged hydrofoil model in following seas. *Ocean Engineering, 31*(5-6), 523-537.

Kim, S.-H., & Yamato, H. (2005). The estimation of wave elevation and wave disturbance caused by the wave orbital motion of a fully submerged hydrofoil craft. *Journal of Marine Science and Technology, 10*(1), 22-31.

Koutsourakis, N., Bartzis, J. G., & Markatos, N. C. (2012). Evaluation of Reynolds stress, k-ε and RNG k-ε turbulence models in street canyon flows using various experimental datasets. *Environmental fluid mechanics*, 1-25.

Ma, S., Wang, R., Zhang, J., Duan, W., Ertekin, R. C., & Chen, X. (2016). Consistent formulation of ship motions in time-domain simulations by use of the results of the strip theory. *Ship Technology Research, 63*(3), 146-158.

Manual, F. D. U. (2011). Flow3D User Manual, v9. 4.2, Flow Science. *Inc., Santa Fe, NM*.

Matveev, K., & Duncan, R. (2005). *Development of the tool for predicting hydrofoil system performance and simulating motion of hydrofoil-assisted boats.* Paper presented at the High Speed and High Performance Ship and Craft Symposium, Everett/WA: ASNE, USA.

McCauley, J. L. (2018). Hydrodynamic Lift on Boats. *arXiv preprint arXiv:1808.03313*.

Reguram, B. R., Surendran, S., & Lee, S. K. (2016). Application of fin system to reduce pitch motion. *International Journal of Naval Architecture and Ocean Engineering, 8*(4), 409-421.

Seif, M., Mehdigholi, H., & Najafi, A. (2014). Experimental and numerical modeling of the high speed planing vessel motion. *Journal of Marine Engineering & Technology, 13*(2), 62-72.

Sun, X., Yao, C., Xiong, Y., & Ye, Q. (2017). Numerical and experimental study on seakeeping performance of a swath vehicle in head waves. *Applied Ocean Research, 68*, 262-275.

Vakilabadi, K. A., Khedmati, M. R., & Seif, M. S. (2014). Experimental study on heave and pitch motion characteristics of a wave-piercing trimaran. *Transactions of FAMENA, 38*(3), 13-26.

Yakhot, A., Rakib, S., & Flannery, W. (1994). Low-Reynolds number approximation for turbulent eddy viscosity. *Journal of scientific computing, 9*(3), 283-292.

Yakhot, V., & Orszag, S. A. (1986). Renormalization group analysis of turbulence. I. Basic theory. *Journal of scientific computing, 1*(1), 3-51.

Yao, C.-B., Sun, X.-S., Wang, W., & Ye, Q. (2017). Numerical and experimental study on seakeeping performance of ship in finite water depth. *Applied Ocean Research, 67*, 59-77.

CHARACTERISTIC OF SPENT BLEACHING EARTH SUBSTITUTION IN LIMESTONE AS LANDFILL MATERIAL

Andriyan Yulikasari., Nagari Meidi YT., Yusroni SA., and Widya Utama*
Department of Geophysical Engineering, Institut Teknologi Sepuluh Nopember, Indonesia
*email: widya@geofisika.its.ac.id

ABSTRACT

The substitution SBE in limestone can significantly improve the characteristics of limestone as a landfill material, especially in increasing the CBR hardness value without changing the limestone grain size distribution. This is because SBE acts as filler in the SBE-limestone mixture. The existence of SBE in the mixture does not change the value of the mixture plasticity index, because SBE and limestone are both not plastic. SBE material can be used as substitution material (matrix material) up to 30% by weight in the SBE-limestone mixture. The role of SBE as a filler becomes very important in mixed materials for non-limestone structural material requirements, especially for matrix material sizes from 0.4 to 10 mm or sand to gravel. Of course, more research is needed on the physical and mechanical characteristics of mixed materials due to the use of SBE as a filler in matrix multi grand size (sand to gravel).

Keywords : *SBE, Limestone, Substitution, Filler, Landfill.*

INTRODUCTION

Spent bleaching earth is a waste from the production process of the palm oil processing industry so that it is included in the category of waste resulting from processing animal/ vegetable fats and their derivatives. The waste based on Indonesian Government Regulation No. 85 Year 1999 includes B3 waste (Hazardous and Toxic Materials) from specific sources. According to PP 74/2001, hazardous and toxic materials (B3) are materials whose properties, concentration, and / or quantity, either directly or indirectly, can pollute and or damage the environment, and or can endanger the environment, health, survival humans and other living things (Damanhuri, 2009).

SBE contains high residual or organic compounds within in range of 20-40% from Palm Oil Refinery. The main chemical composition SBE is SiO_2 (>50%) but has lower CaO (10%) compare to limestone (Yunus et al., 2019). The physical properties of SBE according to (Farahiyah et al., 2020) claim that mean particle size SBE was 29,3μm, the particle size of SBE was 80,42μm and the specific gravity of SBE was 1,93.

However, SBE can be recycled or processed into materials that are used as landfill material, as what written at Minister of Environment and Forestry Regulation Number 10 of 2020. SBE can be recycled and used as material for building such as brick, concrete, cement replacement, and so on. On the previous research, showed that the compressive strength of concrete blocks made from SBE which was extracted without using aggregates, both domato soil, river sand, and split gravel, did not fulfill the SNI and PUBI requirements. However, the composition of the SBE 25% is better than the SBE composition of 50% and

75% (Pojoh, 2016). On the other research has been mentioned that the composition used of SBE waste which results in compliance with the required compressive strength standard is SBE with a composition of 15% and 25%, and the composition of more than 25% SBE can't be used as a brick (Abrar,2019). (Sharom, 2016) determines that SBE could be a potential innovation product for construction materials. This study is to investigate the optimum SBE as replacement through several mixtures of foamed concrete. The best performance properties to replace cement are 30% compared to control foamed concrete. The main aim of this research is to determine the percentage of SBE substitution in limestone used as a landfill material. Therefore, in this study 30, 40, 50% of SBE was used to partially replace/substitution limestone

METHODS

The material that used in this study is limestone and SBE. The variations of the mixture are made based on the ratio of % by weight (Table I).The SBE in this study has been through an extraction process, so that the value of the oil content is below than 3%. The testing methods used are as follows :

TABLE I
LIMESTONE AND SBE MIXTURE

No	SBE (%)	Limestone (%)
1	0	100
2	30	70
3	40	60
4	50	50
5	100	0

1. Analysis of Sieves

Sieves testing is a method for calculating grain size distribution based on soil sedimentation in water. Dry the material in the sun until it is completely dry then sift until the fraction filter is held and pass filter No. 200.

2. Atterberg Limits Testing (Liquid Limit and Plastic Limit)

The condition of the material that has the lowest water content where the soil behaves from plastic to liquid conditions or the state of the material that has a water content between plastic and liquid. The liquid limit is the water level when the nature of the soil at the limit from the liquid state becomes plastic (SNI 1966: 2008). Methodology: soil samples that have been inserted into the cassagrande tool, made a gap in the middle with a standard grooving tool then the cassagrande tool is rotated at a speed of 2 beats per second and the height Of the fall is 10 mm, so that on the 25th tap of the soil sample that is scratched with the grooving tool close as far 0.5 inch.

Plastic limit is the lowest limit of water content conditions when the soil is still in plastic conditions (SNI 1966: 2008). Methodology: sift the soil sample with sieve No. 40 and then take a soil sample of about the size of the thumb and then roll it on a glass plate until it reaches a diameter of 3 mm until it cracks or break. Put the test object into a container then the weigh it. The last is to determine the water content of the test specimen.

3. Proctor Testing

Proctor testing is intended to determine the maximum soil through collision, which is to find out the relationship between water content and soil density. Take a soil sample of 2.5 kg and add water little by little until evenly mixed and then clenched it by hand. When the hand is opened, the ground is not crushed and sticky in the hands. By using Proctor Standard, the land is divided into 3 parts. The first part put into the mold crushed 25 times until evenly distributed. The same way is done for the second and third parts.

4. CBR (California Bearing Ratio) Laboratory Testing

CBR (California Bearing Ratio) is a method for assessing soil strength. The CBR value is the ratio number (in percent) between the pressure needed to penetrate the ground with a round piston that is 3 inci2 wide and the penetration speed of 0.05 inches/ minute to the pressure needed to penetrate a certain standard material.

RESULT AND DISCUSSION

The test method of substitution SBE in limestone has been carried for several variations in the composition of SBE - limestone mixture. The test methods are intended to obtain physical and mechanical characteristics of the material based on 4 test methods that is, the sieve test, Atterberg test, Proctor test, and CBR test.

The result of the sieve test shown that the distribution of SBE grain sizes (more than 90%) pass from sieve number 200. This indicates that the grain size of the SBE material is smaller than 0.075 mm. The grain size of limestone varies from larger than 1 mm (65% in distribution) to less than 0.075 mm (35% in distribution).

Table II indicated that the substitution SBE in limestone composition does not change the grain size distribution of the limestone. Since SBE act as filler in the mixture so the substitution in limestone does not affect the gradation of limestone. Even the substitution of SBE up to 50% in the mixed composition does not change the size distribution of limestone grain size. In its application for landfills, in terms of grain size distribution, SBE substitution in limestone can be used up to 50% of its weigh but the best gradation is shown in the 30% SBE substitution.

The Atterberg test is used to determine the characteristics of plasticity material. The result of Atterberg test is indicated that both of the initial material is non-plastic (PI = 0%) (Fig.1). Therefore, the two initial materials are non-plastic, so the mixture will automatically be non-plastic. Index Plasticity (PI) can indicate the plasticity condition of a material or the ability of grains to deformation without change in shape or volume. According to SNI-03-6797-2002 (AASHTO M145) that the maximum PI value for landfill is 6%, so the initial material and the mixture material can be used as a landfill material. The Soil Activity (A) is used as an index to identify the ability of soil to swelling. Soil activity (A) is a comparison between the Plasticity Index (PI) with a percentage of grains smaller than 0.002 mm (Fig.2). Based on SNI that the maximum Soil Activity (A) for landfill is 1,25%, so the result of Soil Activity (A = 0%) test from all materials indicate that the materials can be used for landfill (Fig.2).

TABLE II
SIEVE TEST RESULT OF SBE SUBSTITUTION IN LIMESTONE

Grand Size	Unit	Initial material		Mixture		
		SBE	LM	LM 50% vs SBE 50%	LM 60% vs SBE 40%	LM 70% vs SBE 30%
Gravel (2-64 mm)	%	0	15,6	18,88	17,01	16,96
Sand (1-0.125 mm)	%	4,28	49,3	46,71	32,05	34,14
Clay and Silt (0.04-<1/256 mm)	%	95,7	35,1	34,41	50,94	48,9
AASHTO		A-4	A-4	A-2-4	A-4	A-4

TABLE III
PROCTOR TEST RESULT OF SBE SUBSTITUTION IN LIMESTONE

	Unit	SBE 100%	LM 100%	LM 50% vs SBE 50%	LM 60% vs SBE 40%	LM 70% vs SBE 30%
Specific Gravity		2,62	2,62	2,63	2,62	2,62
OMC	%	33	14,7	16,2	16,9	15,9
γd max	gr/cc	1,04	1,77	1,45	1,42	1,53

Proctor testing aims to obtain the maximum dry weight and optimum water required to compact a material. The compaction is intended to improve the quality of the soil by increasing the shear strength of the soil, minimizing settlement, reducing permeability, and controlling changes in relative volume due to the shrinkage-swelling of soil. Based on the general guidelines for the selection of landfill materials suggested by Gregg (1960), it is stated that limestone is included in the moderate to very good material category while SBE is included in the not satisfactory material category. Based on the test results (Table 3), the substitution of SBE in limestone shows a value that tends to decrease compared to the initial material value (LM 100%), but the quality of the material is still in the good category for landfills. This case is indicated from dry density value, SBE dry density is 40% lower than limestone but the substitution SBE in limestone until 50% only reduce the value of dry density limestone by 16%, not a significant change in use. The best compaction value is obtained from SBE 30% - limestone 70% by weight material with a maximum dry weight value of 1,53 gr/cc and an optimum moisture content of 15,9%, so it is categorized as a poor to good performance.

CBR testing is used to evaluate the potential strength of the landfill material. The test was conducted using SNI standard 03-1744-2012 referring to AASHTO T193-99 (2007). The greater of CBR value indicates the better carrying capacity of the land. But this can be influenced by several factors. The factor which greatly influences the CBR value is material compaction. The greater of maximum dry weight and optimum moisture content in the compaction process (see Table 3), then the CBR value will also be greater. SNI Standard CBR value for selected fill material is at least 10%, for ordinary fill material a minimum value at least 6%. The CBR value of the SBE substitution of the limestone obtained is greater than the CBR value of the initial limestone, however this condition is inversely proportional to the maximum dry weight value and the optimum water content is much lower than the initial limestone (Fig.3).

Based on Fig. 3, the best CBR value is obtained at SBE substitution of 30% in limestone resulting in a CBR value of 43.20. This value is greater than the initial material CBR value (LM 100%). This is indicated by the presence of SBE filling the pore in the limestone causing the soil to be more compact, but the compaction value is smaller due to the nature of SBE which cannot absorb water well. The nature of SBE is due to the gradation of this material which is homogeneous and fine.

CONCLUSION

SBE substitution in limestone as a landfill material can be used up to 30% by weight based of the test result. The substitution SBE in limestone does not change the grain size composite material even up to 50% by weight substitution. SBE and limestone are non-plastic material, both of them do not have a swelling or shrinking characteristic due the changes in water saturation value in the

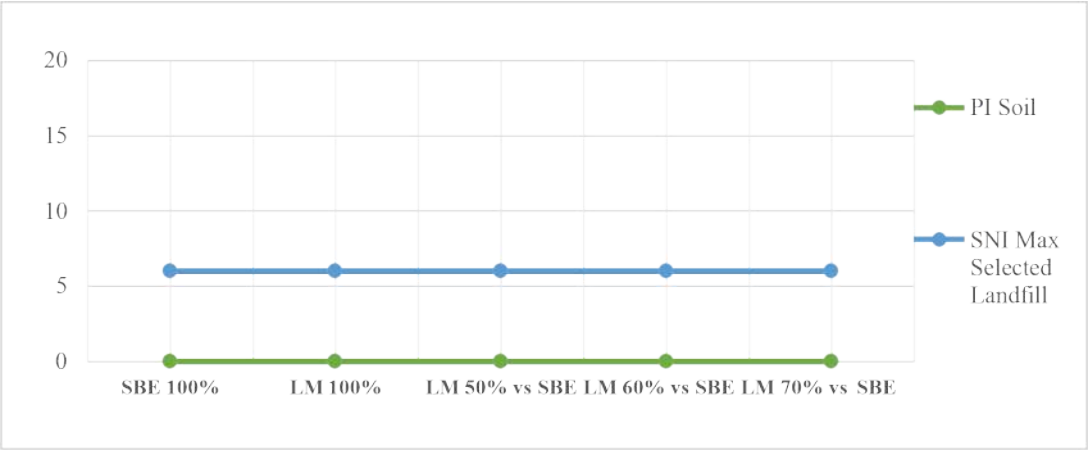

Fig. 1. Index plasticity (PI) test

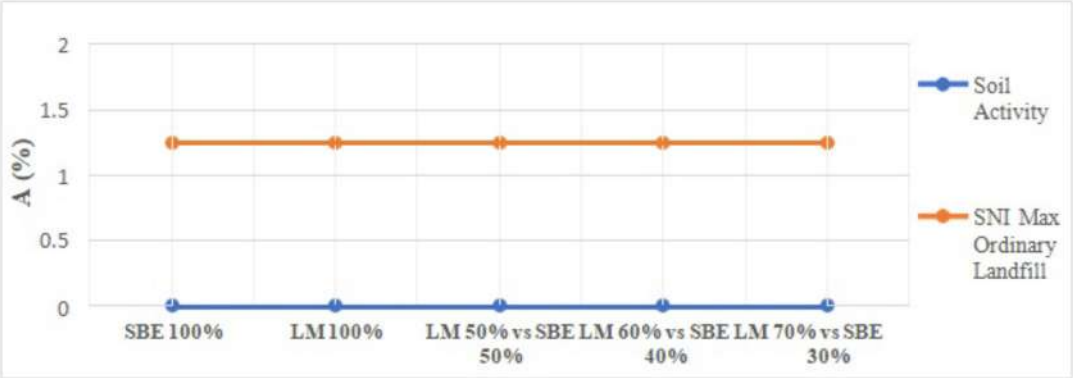

Fig. 2. Soil activity (A) test result

material and according to SNI-03-6797-2002 (AASHTO M145) SBE substitution in limestone can be used as a landfill material. The Proctor test shows that the SBE dry density level is 40% lower than limestone.

However, SBE substitution of up to 50% by weight in limestone only reduces the value of limestone dry density by 16%, not a significant change in use. So, the substitution SBE in limestone up to 50% does not significantly change the characteristics of the limestone-based landfill material with moderate performance. The best performance is obtained at 30% SBE substitution. SBE substitution can increase the CBR value of the mixture up to 200% or 2 times the original CBR limestone value. So as a fine material (90% distribution in clay and silt grand size), SBE acts as a filler in the SBE-limestone mixture for landfill material.

REFERENCES

Abrar, Aidil and Nuryasin Abdillah. Studi Eksperimen Pemnafaatan Limbah Spent Bleaching Earth (SBE) sebagai Bahan Pembuat Bata. Siklus: Jurnal Teknik Sipil 5 (2): 70-78. https://doi.org.10.31849/siklus.v5i2.3223.

Ajemba, R.O., dan Onukwuli, O.D., 2013, Nitric Acid- Activated Nteje Clay: Structural and Bleaching Properties, International Journal of Engineering, 26 (5): 495-500.Damanhuri, E. 2010. Diktat Kuliah: Pengelolaan Bahan Berbahaya Dan Beracun (B3). Teknik Lingkungan ITB.

Damayanti, Cendy, 2019, Pengaruh Jenis dan Konsentrasi Asam Terhadap Proses Reaktiviasi Spent Bleaching Earth (SBE) Hasil Samping Produksi Biosolar, Skripsi Universitas Lampung, Bandar Lampung.

East Java Provincial Government, General

Specifications of the Public Works Department of Highways in East Java Province, 2018.

Farahiyah, R., Rahman, A., Asrah, H., Rizalman, A. N., Abdul, K., & Rajak, M. A. A. (2020). Study of Eco- Processed Pozzolan Characterization as Partial Replacement of Cement. 8(3), 967–970.Farihahusnah, H., Mohamed, K. A., dan Wan, M. A. W. D., 2011, Textural Characteristics, Surface Chemistry and Activation of Bleaching Earth, Indonesian Journal Chemical Science, 5 (3): 202-205.

Helbianurramdan, Noor Hindryawati, R.R Dirgarini Julia N.S, 2017, Aktivasi Deoiled Spent Bleaching Earth (DSBE) dengan Menggunakan Metode Ultrasonik untuk Mengadsorpsi Ion Logam Pb2+, Jurnal Atomik: 02, Hal. 241-247.National Standardization Agency, Test Method for Determination of Plastic Limits and Soil Plasticity Index, SNI 1966-2008.

National Standardization Agency, Light Density Test Method for Land, SNI 1742-2008.

National Standardization Agency, Laboratory CBR Test Method, SNI 03-1744-2012.

National Standardization Agency, Test Method for Analysis of Soil Grain Size, SNI 3423-2008.

Pojoh, Broerie and A. Luther Ola. 2016. Handling of Spent Bleaching Earth Waste Pile of Coconut Oil Factory Through "Batako" Making. Jurnal Penelitian Teknologi Industri 8 (1): 1- 10.Farahiyah, R., Rahman, A., Asrah, H., Rizalman, A. N., Abdul, K., & Rajak, M. A. A. (2020). Study of Eco-Processed Pozzolan Characterization as Partial Replacement of Cement. 8(3), 967–970.

Sharom, N. B. I. N. (2016). Iii Performance of Eco Process Pozzolan Foamed Concrete As Cement Replacement. January.

Utama, Widya, 2019, Karakterisasi Subsitusi EPP pada Campuran Limestone dan Mud untuk Tanah Urugan. ITS, Surabaya.

Wahyudi, MY. 2000. Studi Penggunaan kembali Bleaching Earth Bekas sebagai Adsorben dalam Proses Refining CPO. Tesis Magister. Program Studi Teknik Lingkungan. Institut Teknologi Bandung, Bandung.

Yunus, E., Asrah, H., & Rizalman, A. N. (2019). Compressive Strength of Eco-Processed Pozzolan Concrete under Chloride and Sulphate Exposure. 1(1), 1–9.

JMEST
Volume 1 Issue 1
Sept - Dec 2020
ISSN 2774-5449